

1       **Spatial variation in shallow slow earthquake activity in Hyuga-nada, southwest Japan**

2  
3       Satoru Baba<sup>1,2</sup>, Shunsuke Takemura<sup>1</sup>, Kazushige Obara<sup>1</sup>, Akiko Takeo<sup>1</sup>, Yusuke Yamashita<sup>3</sup>, and  
4       Masanao Shinohara<sup>1</sup>

5  
6       1. Earthquake Research Institute, the University of Tokyo, 1-1-1, Yayoi, Bunkyo-ku, Tokyo,  
7       113-0032, Japan

8       2. Now at Japan Agency for Marine-Earth Science and Technology, 2-15, Natsushima-cho,  
9       Yokosuka, Kanagawa, 237-0061, Japan

10      3. Miyazaki Observatory, Disaster Prevention Research Institute, Kyoto University, 3884 Kaeda,  
11      Miyazaki, Miyazaki, 889-2161, Japan

12  
13      **Abbreviated title:** Spatial variation in slow earthquakes in Hyuga-nada

14  
15      **Corresponding author:** Satoru Baba

16      E-mail: babasatoru@jamstec.go.jp

17      Phone: +81-46-867-9342

18  
19

20 **Summary**

21 Hyuga-nada, off the Pacific coast of Kyushu along the Nankai Trough in southwest  
22 Japan, is one of the most active slow earthquake regions around Japan. We estimated the energies  
23 of shallow tremors and moments of shallow very low frequency earthquakes (VLFs) in Hyuga-  
24 nada using data from a permanent onshore broadband network and temporary ocean bottom  
25 seismometer observations. The energies and moments of these slow earthquakes have a similar  
26 along-strike variation and are generally higher south of the subducted Kyushu-Palau Ridge than  
27 near the top of the ridge. This spatial variation is also related to the characteristics of slow  
28 earthquake migration. The along-strike migration speed was faster at initiation in the south, where  
29 the moments of slow earthquakes are higher. After migration entered the subducted Kyushu-Palau  
30 Ridge, its speed was decelerated with a parabolic pattern and their moments became smaller.  
31 Assuming a constant patch size of slow earthquakes, we estimated that the stress drop of VLFs  
32 in the south of the subducted ridge was approximately three times higher than that near the top of  
33 the subducted ridge. According to our observations and a physical model, this stress drop  
34 difference between adjacent regions may cause parabolic migration. We also estimated the scaled  
35 energy of slow earthquakes from the ratio of the seismic energy rates of tremors to the seismic  
36 moment rates of accompanying VLFs. The spatial variation in scaled energy is not identified  
37 inside the Hyuga-nada. Since the range of scaled energy is similar between the south and near the  
38 top of the subducted ridge, the apparent stress may be similar if the rigidity is the same. The  
39 dominant range of scaled energy of slow earthquakes in Hyuga-nada is  $10^{-11.5}$ – $10^{-8.5}$ . In addition  
40 to having similar or one order smaller values compared to other slow earthquake regions, the  
41 range of scaled energy in Hyuga-nada is broader. This broader range suggests wide range of  
42 characteristic time and various spectral features of slow earthquakes in Hyuga-nada. Based on a  
43 Brownian slow earthquake model, the wide range of characteristic time in this area suggests width  
44 variations of slow earthquake source area.

45

46 **Keywords:** Subduction zone processes, Seismicity and tectonics, Earthquake source observations,  
47 Japan

48

49

## 50 **1. Introduction**

51 After the discovery of tectonic low frequency tremors by Obara (2002), slow  
52 earthquakes, which are fault slips with longer characteristic durations than regular earthquakes  
53 with the same seismic moment (e.g., Ide et al. 2007a; 2008; Ide & Beroza 2023; Wang et al. 2023),  
54 were mainly detected around seismogenic zones on plate boundaries of subduction zones or strike  
55 slip regimes in the world. Seismic slow earthquakes are classified into tremors and low frequency  
56 earthquakes observed in a frequency range of 2–8 Hz (e.g., Shelly et al. 2006) and very low  
57 frequency earthquakes (VLFs) observed in a frequency range of 0.02–0.05 Hz (e.g., Obara &  
58 Ito 2005). Slow slip events (SSEs) are geodetically observed as crustal deformations, with  
59 duration ranging from several days to several years (e.g., Dragert et al. 2001; Hirose et al. 1999).  
60 The focal mechanisms of slow earthquakes in subduction zones are thrust-type and consistent  
61 with those of megathrust earthquakes along plate boundaries (e.g., Ide et al. 2007b; Ito et al. 2007;  
62 Takemura et al. 2019). In addition, slow earthquake activity can reflect the stress conditions on  
63 the plate boundary around the slow earthquake regions (e.g., Obara & Kato 2016). Recent studies  
64 have revealed that slow earthquakes can potentially trigger megathrust earthquakes. An SSE  
65 occurred before the 2011 Tohoku earthquake in Japan (e.g., Kato et al. 2012), the 2012 Nicoya  
66 Peninsula earthquake in Costa Rica (e.g., Voss et al. 2018), and the 2014 Iquique earthquake in  
67 Chile (e.g., Ruiz et al., 2014). Thus, studies of slow earthquakes are important for understanding  
68 the slip behaviours on the plate boundary and the occurrence mechanism of megathrust  
69 earthquakes.

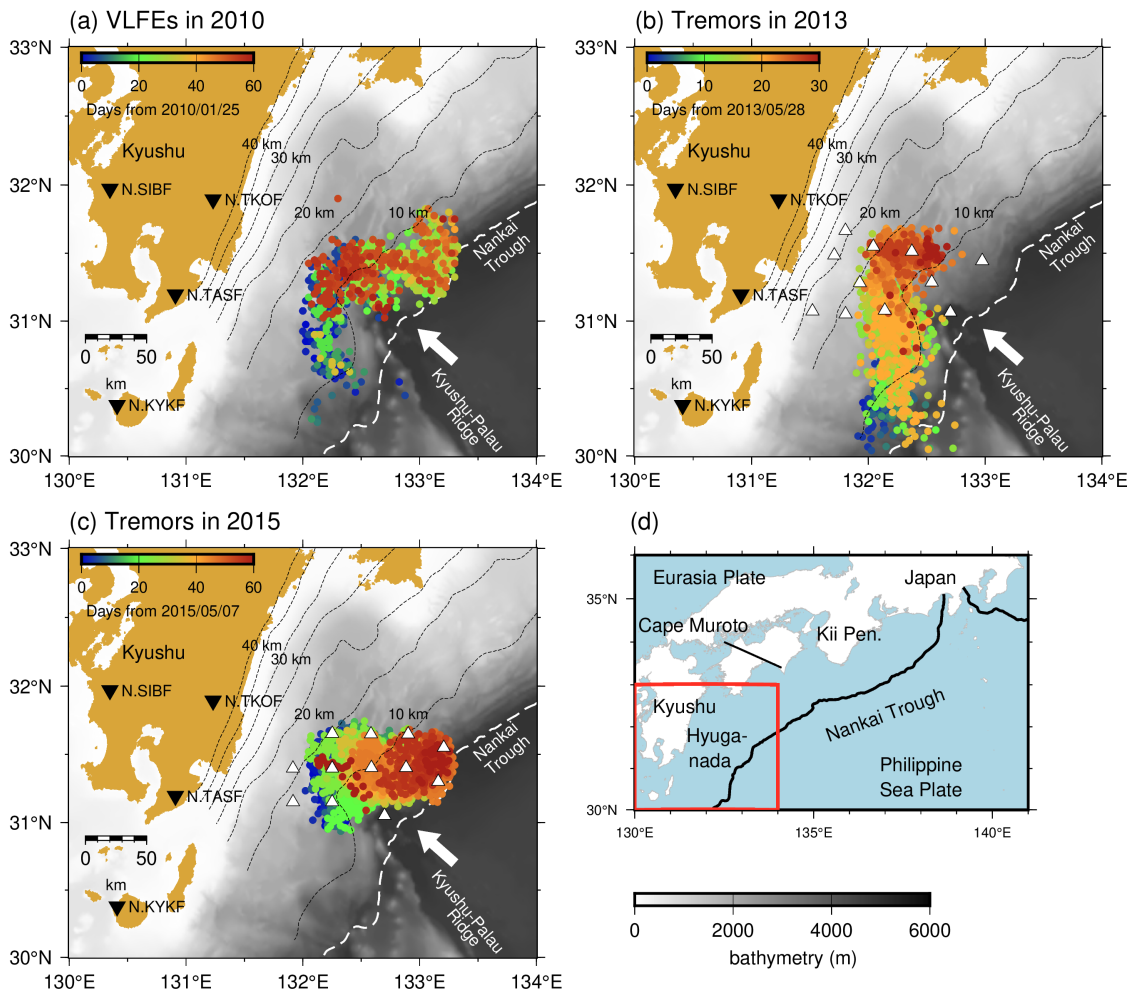
70 Around the Japanese islands, slow earthquakes occur in shallower and deeper extensions  
71 of the seismogenic zone in southwest Japan along the Nankai Trough and in the offshore region  
72 of northeastern Japan along the Japan Trench. In Hyuga-nada, off the Pacific coast of Kyushu,  
73 VLFs are the most active around Japan (Baba *et al.* 2020). In this area, Asano et al. (2015)  
74 reported the migration of shallow VLFs, which can be considered as a proxy for rupture  
75 propagation of an SSE (e.g., Bartlow et al. 2011; Ito et al. 2007), in 2010 (Fig. 1a). VLFs first  
76 migrated from 30.5° N to 31.5° N along the strike direction and changed to along-dip migration  
77 at the subducted Kyushu-Palau Ridge, which is subducting at the Nankai Trough. Although  
78 VLFs are observed by onshore stations owing to the effective propagation of surface waves  
79 along shallower low velocity structures, it is difficult to identify weak signals of shallow tremors  
80 in Hyuga-nada using permanent onshore stations. Yamashita et al. (2015) and Yamashita et al.  
81 (2021) detected shallow tremors and reported their migrations in Hyuga-nada utilizing temporary  
82 ocean bottom seismometers (OBSs) in 2013 and 2015, respectively (Fig. 1b and c). In 2013,  
83 tremors migrated twice from 30.3° N to 31.7° N. In 2015, tremors migrated from west to east,  
84 north of 31° N and extended near the trench axis (Yamashita et al. 2021). The shallow tremors in  
85 Hyuga-nada were temporally correlated with shallow VLFs (Fig. 2). The spatial distributions of

86 tremors in both 2013 and 2015 were contained by those of VLFEs in 2010. Temporary OBS  
87 observations also revealed a high-resolution distribution of VLFEs. Tonegawa et al. (2020)  
88 suggested that the depths of shallow VLFEs near the subducted Kyushu-Palau Ridge are  
89 approximately 5 km different from the surrounding area.

90 The tectonic regime in Hyuga-nada is very characteristic; the Kyushu-Palau Ridge is  
91 subducting and the trench axis bends around the region where the ridge subducts (Fig. 1). In  
92 addition, repeating earthquakes representing quasi-static slips on the plate boundary (e.g., Nadeau  
93 & McEvilly 1999; Uchida et al. 2003) occur in the downdip of shallow slow earthquakes (e.g.,  
94 Igarashi, 2020; Yamashita et al., 2012). Tectonic conditions, such as a subducted ridge or  
95 horizontal heterogeneity of pore fluid pressure around the plate boundary, can affect the source  
96 parameters, such as the moment rate, of slow earthquakes (Baba et al. 2020; Takemura et al.  
97 2022b). To investigate the spatial relationships between slow earthquake activity and tectonic  
98 conditions in Hyuga-nada, we quantitatively estimated the spatial variation in the source  
99 characteristics of slow earthquakes at high spatial resolution using onshore and offshore data.

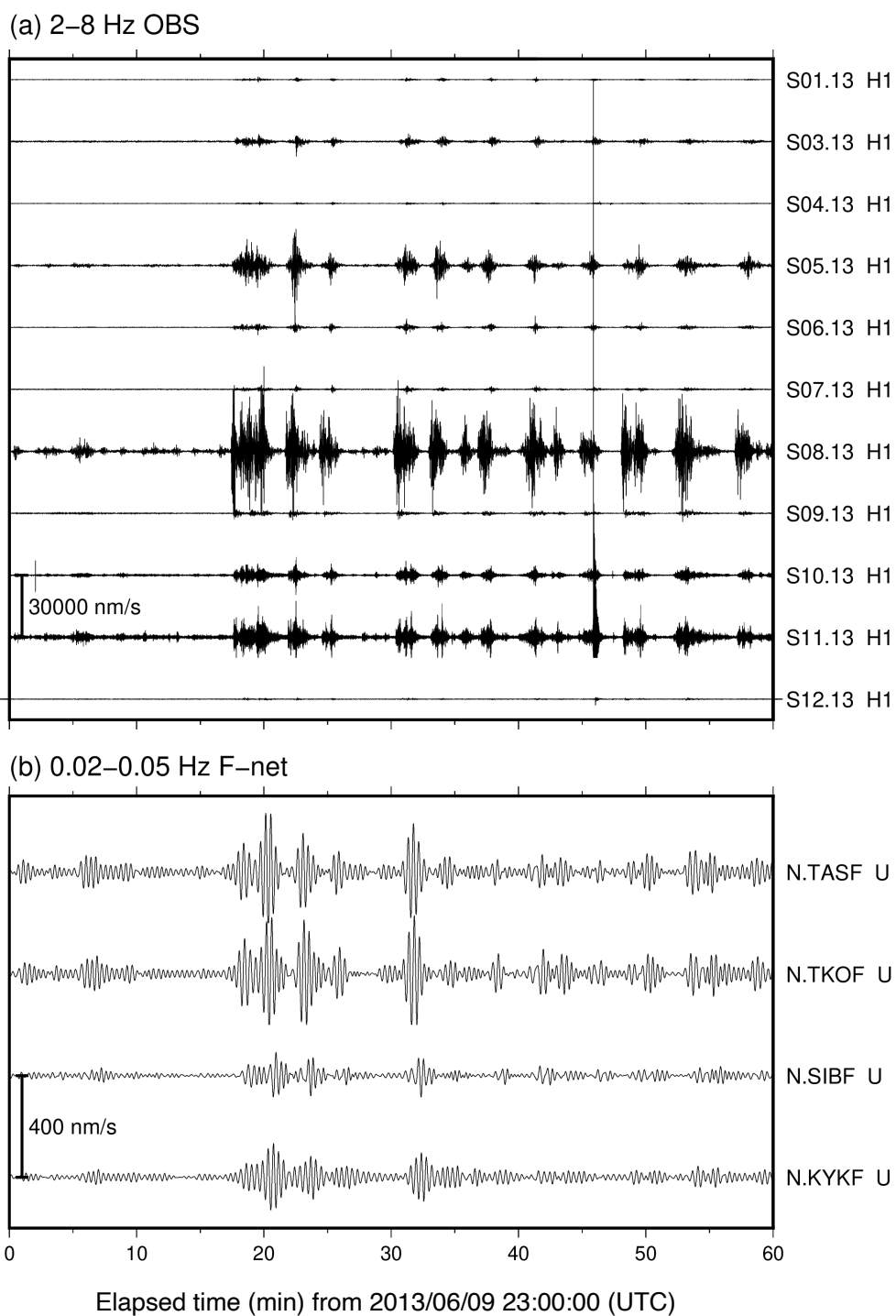
100 As the quantitative indicators of source characteristics, we focus on the energy rate  
101 functions of tremors, moment rate functions of VLFEs, and the scaled energy. Recently, slow  
102 earthquake signals have been also detected in the microseism frequency band between tremors  
103 and VLFEs (Kaneko et al. 2018; Masuda et al. 2020; Yamashita et al. 2021); therefore, slow  
104 earthquakes are assumed to be broadband phenomena (Ide & Maury, 2018). Ide et al. (2008)  
105 demonstrated the seismic energy rates of slow earthquakes in 2–8 Hz are proportional to the  
106 seismic moment rates and evaluated the scaled energy of slow earthquakes by the ratio between  
107 tremor energy rate and the accompanying VLFE moment rate. Scaled energy has been used for  
108 the purpose of comparing dynamic characteristics of seismic events (Kanamori & Rivera 2006).  
109 If the rupture process of seismic events is self-similar, the scaled energy is constant. Previous  
110 studies demonstrated that scaled energy of slow earthquakes is  $10^{-10}$ – $10^{-8}$  and 4–5 orders smaller  
111 than that of regular earthquakes (e.g., Ide et al. 2008). Yabe et al. (2019) and Yabe et al. (2021)  
112 estimated the scaled energy of shallow slow earthquakes along the Nankai Trough and along the  
113 Japan Trench, respectively, and suggested the relationship between scaled energy distribution and  
114 geological condition. To investigate the characteristics of broadband slow earthquakes as well as  
115 the spatial relationships between slow earthquake activity and tectonic conditions, we evaluated  
116 the energy rate functions of tremors, the moment rate functions of VLFEs, and the scaled energy  
117 of the slow earthquakes in Hyuga-nada at a high spatial resolution using onshore and offshore  
118 data.  
119





120  
121  
122  
123  
124  
125  
126  
127  
128  
129  
130  
131  
132  
133  
134  
135

**Figure 1.** Slow earthquake activity in Hyuga-nada. Coloured dots are epicentres of (a) shallow VLFES in 2010 detected by Asano et al. (2015), (b) shallow tremors in 2013 detected by Yamashita et al. (2015), and (c) shallow tremors in 2015 detected by Yamashita et al. (2021). The colours of dots correspond to days from the first activity for each tremor episode. Blue and red dots indicate epicentres of tremors that occurred at the beginning and end of the migration episode, respectively. White triangles represent the locations of the OBSs utilized in the shallow tremor analysis. Inverted triangles exhibit the locations of the F-net stations utilized in the shallow VLFE analysis. White arrows indicate the direction of the motion of the Philippine Sea Plate relative to the Eurasia Plate (NUVEL-1A; DeMets et al., 1994). White dashed lines represent the trench axis. Background grey scale denotes the bathymetry (ETOPO1; Amante & Eakins 2009). Dashed contours indicate the isodepth at the top of the Philippine Sea plate in intervals of 5 km (Nakanishi et al. 2018). (d) Tectonics of Hyuga-nada. The area surrounded by the red rectangle is shown in Figs. 1a-c. Black lines represent the boundaries between the plates.



136

137 **Figure 2.** Example of one-hour records for (a) shallow tremors in a frequency range of 2–8 Hz at  
138 OBSs and (b) shallow VLFES in a frequency range of 0.02–0.05 Hz at F-net stations.

139

140

141 **2. Data and Method**

142 **2.1. Estimation of energy rate functions of tremors**

143 For the analysis of tremors, we evaluated the energy rate functions of tremors located  
 144 by Yamashita et al. (2015; 2021). We used 360 s broadband (NK1508 and NK1510 in 2015), 1  
 145 Hz (S06.13, S09.13 in 2013 and others in 2015) and 4.5 Hz (others in 2013) short-period OBS  
 146 records of temporary seismological observations in Hyuga-nada. 11 and 12 OBSs were installed  
 147 for observations from April 17 to July 4, 2013 (Yamashita et al. 2015) and from January 1, 2015  
 148 to January 1, 2016 (Yamashita et al. 2021), respectively. The sampling rates were 200 Hz (S05.13,  
 149 S06.13, S08.13, and S09.13 in 2013 and all OBSs in 2015) or 128 Hz (other OBSs in 2013).  
 150 Analog seismic signals were digitized using a 16-, 20-, or 24-bit A/D converter. After instrumental  
 151 responses were removed, a bandpass filter was applied in a frequency range of 2–8 Hz. Then, the  
 152 vertical and horizontal components of the root-mean-square (RMS) velocity envelopes were  
 153 calculated with a smoothing time window of 5 s. The envelopes were resampled at one sample  
 154 per second. Examples of envelope waveforms of a tremor obtained by the RMS of the sums  
 155 squared seismograms of two horizontal components are displayed in Fig. 3. Since OBSs are often  
 156 installed on soft sediments, amplitudes of seismic waves are more amplified compared to onshore  
 157 stations. We therefore selected a permanent onshore station N.TASF from the F-net broadband  
 158 seismograph network (Aoi *et al.* 2020) as a reference station, because F-net stations are installed  
 159 at inland outcrop rock sites (Aoi et al., 2020) and the site amplification factors between F-net  
 160 stations are very similar (Takemoto *et al.* 2012).

161 We estimated the site amplification factors of the vertical and horizontal components  
 162 at each OBS relative to N.TASF at 2–8 Hz and the quality factor of the *S*-wave attenuation ( $Q$ )  
 163 by utilizing the information of the maximum *S*-wave amplitudes of intraslab regular earthquakes  
 164 following the method of Yabe et al. (2019). The maximum *S*-wave amplitude of the  $i$ -th  
 165 earthquake at the  $j$ -th station ( $A_{ij}$ ) is expressed by the following relationship:

166 
$$\ln(A_{ij}) = \ln(S_i) - \ln(\sqrt{4\pi}L_{ij}) - \frac{\pi f_c Q^{-1}}{V_s} L_{ij} + \ln(C_j) \quad (1)$$

167 where  $S_i$  is the size of the  $i$ -th seismic source,  $L_{ij}$  is the distance between the hypocentre of the  $i$ -  
 168 th earthquake and the  $j$ -th station,  $f_c$  represents the central frequency (5 Hz in this study),  $V_s$  is the  
 169 *S*-wave velocity (assuming 3.5 km/s; after Yabe et al, 2019; 2021), and  $C_j$  is the site amplification  
 170 factor.  $Q^{-1}$  represents apparent *S*-wave attenuation, including intrinsic and scattering attenuations.  
 171 The attenuation by geometrical spreading corresponds to the second term of the right-hand side  
 172 of the equation (1). We measured the maximum *S*-wave amplitudes of regular earthquakes more  
 173 than 5 km deeper than the plate boundary of the Japan Integrated Velocity Structure Model  
 174 (JIVSM; Koketsu et al. 2012) with magnitudes larger than 2.5 listed in the regular earthquake  
 175 catalogue of the Japan Meteorological Agency (Fig. S1). We defined the maximum envelope

176 amplitude of the time window from 2 s before to 50 s after the arrival time at each OBS as the  
 177 maximum  $S$ -wave amplitude. To estimate the site amplification factor of  $j$ -th station relative to a  
 178 reference station ( $j_0$ ), taking the difference of equation (1) for  $i$ -th event at  $j$ -th and the reference  
 179 station:

$$180 \quad \ln\left(\frac{A_{ij}}{A_{ij_0}}\right) + \ln\left(\frac{L_{ij}}{L_{ij_0}}\right) = -\frac{\pi f_c Q^{-1}}{V_S}(L_{ij} - L_{ij_0}) + \ln\left(\frac{C_j}{C_{j_0}}\right). \quad (2)$$

181 The site amplification factor relative to N.TASF and  $Q^l$  at each OBS was estimated by solving  
 182 Equation (2) using the least-squares method. Following Yabe et al. (2019), we set the site  
 183 amplification factor at the reference station N.TASF as 2 to consider the free-surface effect. In the  
 184 following steps, we utilized the RMS of the sums of the squared three-component seismograms  
 185 with a smoothing time window of 5 s after site correction by implementing the site amplification  
 186 factors displayed in Fig. 4. After correcting the site amplification factors, the amplitudes were  
 187 normalized by the site conditions at the reference onshore station, N.TASF. We also evaluated the  
 188 average of  $Q^l$  solved at each OBS in Equation (2) as  $(3.4415 \pm 0.9585) \times 10^{-3}$ . We adopted this  
 189 value to estimate the energy rate functions of the tremors.

190 We calculated the energy rate functions of the tremors by implementing the site  
 191 amplification factors and  $Q^l$  estimated by the above procedures. The energy rate function of a  
 192 tremor ( $E_j(t)$ ), estimated from the amplitudes of the  $j$ -th station, was calculated using the following  
 193 equation:

$$194 \quad E_j(t) = 2\pi V_S r_j^2 \rho A''_j(t + t_j) \exp(2\pi f_c Q^{-1} t_j) \quad (3)$$

195 where,  $A''_j(t)$  is the amplitude of envelopes after the site-correction at the  $j$ -th station,  $r_j$  is the  
 196 hypocentral distance from the tremor source to the  $j$ -th station,  $t_j$  is the travel time from the tremor  
 197 source to the  $j$ -th station, and  $\rho$  is the density (assuming  $2,700 \text{ kg/m}^3$  after Yabe et al, 2019; 2021).  
 198 The epicentral locations of the tremors were set at those located by Yamashita et al. (2015; 2021).  
 199 The depth of the tremors was set at the plate boundary of the JIVSM (Koketsu et al. 2012). To  
 200 calculate the energy rate function, the time windows were set at 240 s, which started 60 s before  
 201 the time window of the tremors set by Yamashita et al. (2015; 2021). We stacked the energy rate  
 202 functions of a tremor for each station and estimated the average energy rate function  $E_{ave}(t)$   
 203 divided by the number of used stations. We calculated the cross-correlation coefficients (CCs) of  
 204 the energy rate functions of all station pairs in Fig. 4 and further utilized the stations whose CCs  
 205 exceeded 0.6 with at least one other station when stacking the energy rate functions.

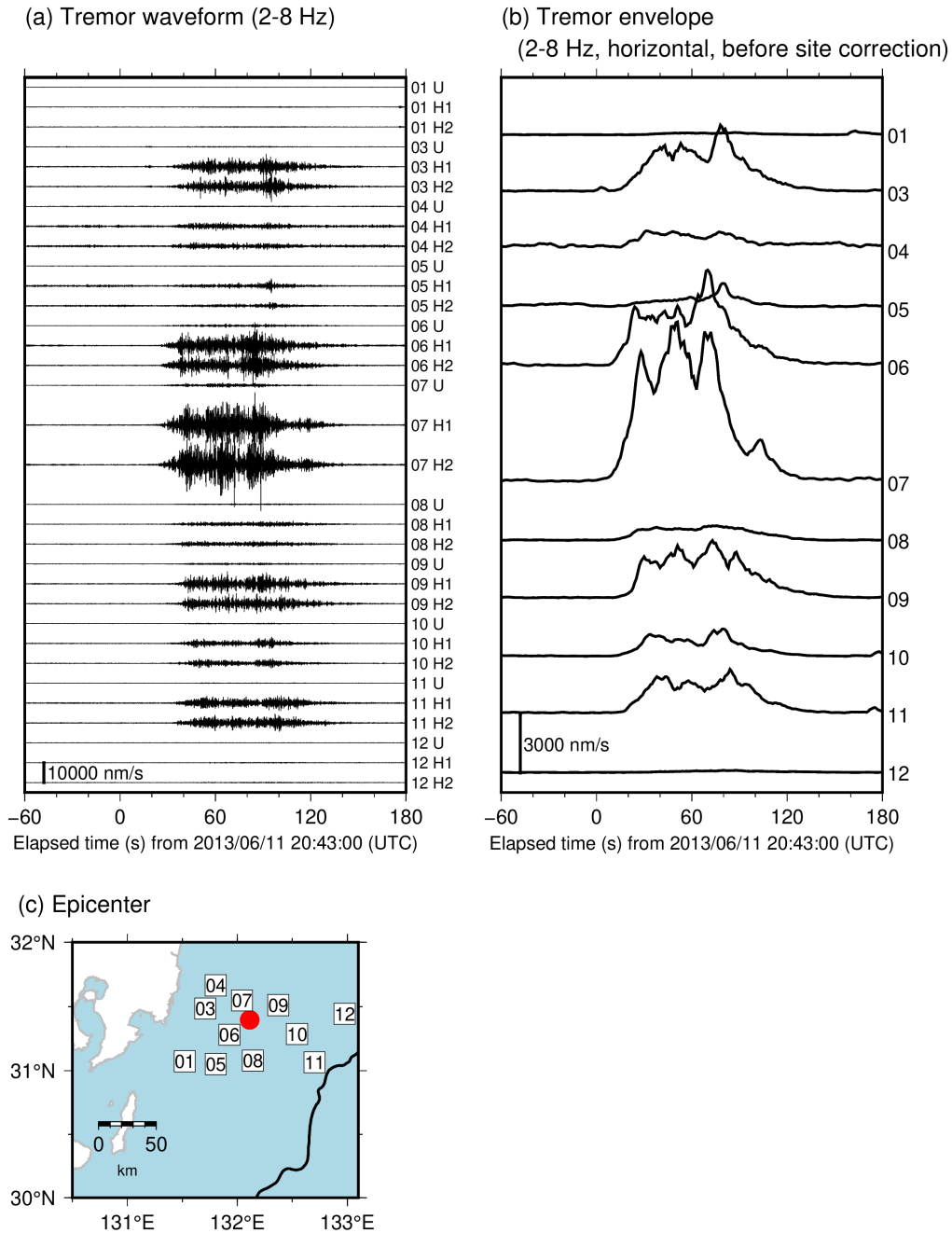
206 The seismic energy  $W$  of a tremor is calculated by integrating  $E_{ave}(t)$  in the time range  
 207  $t_1-t_2$ :

$$208 \quad W = \int_{t_1}^{t_2} E_{ave}(t) dt. \quad (4)$$

209 The integration range is the period when the values of  $E_{ave}(t)$  exceed 20% of the maximum

210 value of  $E_{\text{ave}}(t)$  (red line in the stacked energy rate function of Fig. 5). The duration of a tremor  
211 was defined as  $t_2 - t_1$ . The dominant range of tremor duration is 30–100 s. The seismic energy  
212 rate of the tremor was estimated by dividing the seismic energy by the duration. To evaluate the  
213 uncertainty of estimated energies, we calculated the standard deviation of the logarithm of  
214 energies estimated from each OBS data. The uncertainty of tremor energies is 0.5–1 order (Fig.  
215 S3a).

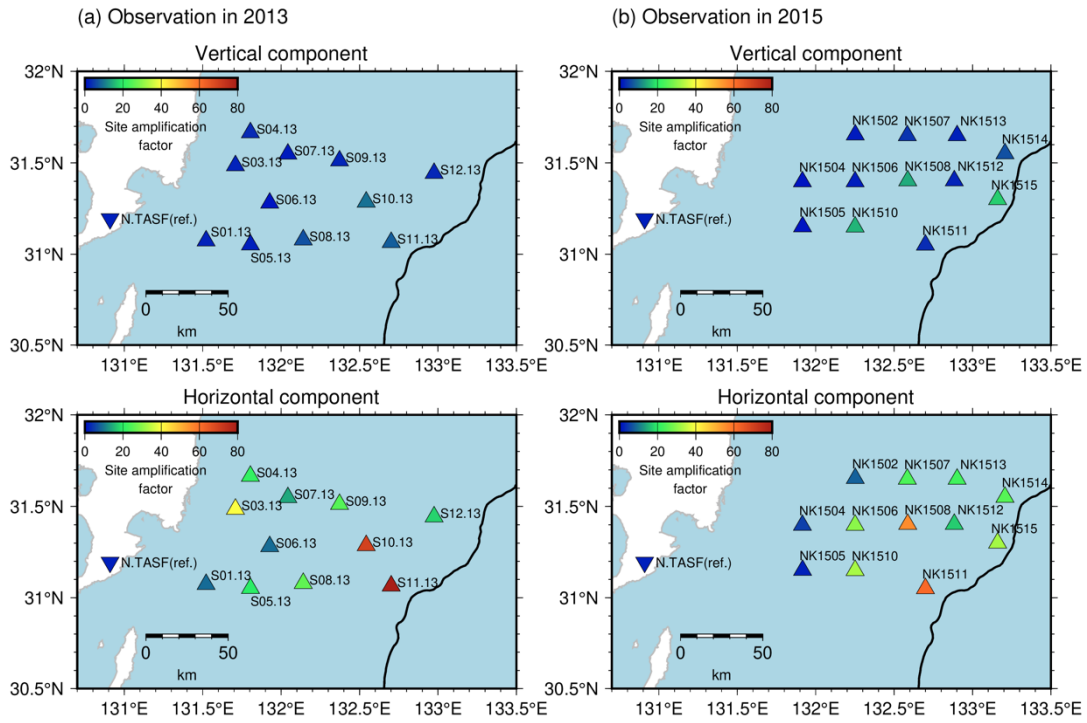
216 To validate the method of seismic energy estimation, we estimated seismic energies of  
217 regular earthquakes in the 2015–2016 observation by using the equations (3) and (4) (Fig. S4).  
218 The earthquakes in the area of 131.0°E–133.5°E and 30.0–32.0°N with moment magnitudes larger  
219 than 4 by moment tensor analysis by F-net site  
220 (<https://www.fnet.bosai.go.jp/event/search.php?LANG=en>) were selected. In previous studies,  
221 scaled energies of regular earthquakes evaluated by the ratio of seismic energy to seismic moment  
222 are estimated to be approximately  $3 \times 10^{-5}$  (e.g., Ide & Beroza 2001). The scaled energies of most  
223 regular earthquakes shown in Fig. S4a are in the range of  $10^{-5}$ – $10^{-4}$  (Fig. S4b). It indicates that  
224 this method can estimate seismic energies on an order scale.  
225



226

227 **Figure 3.** Example of (a) waveforms of a tremor in a frequency range of 2–8 Hz, and (b) envelopes  
228 obtained by the root-mean-square of sums squared seismograms of two horizontal components.  
229 Waveforms are displayed from 20:43:00 (UTC), June 11, 2013. (c) Red circle depicts the  
230 epicentre of the tremor displayed in in Fig. 3a and b. Black line represents the trench axis. Squares  
231 indicate the locations of OBSs.

232



233

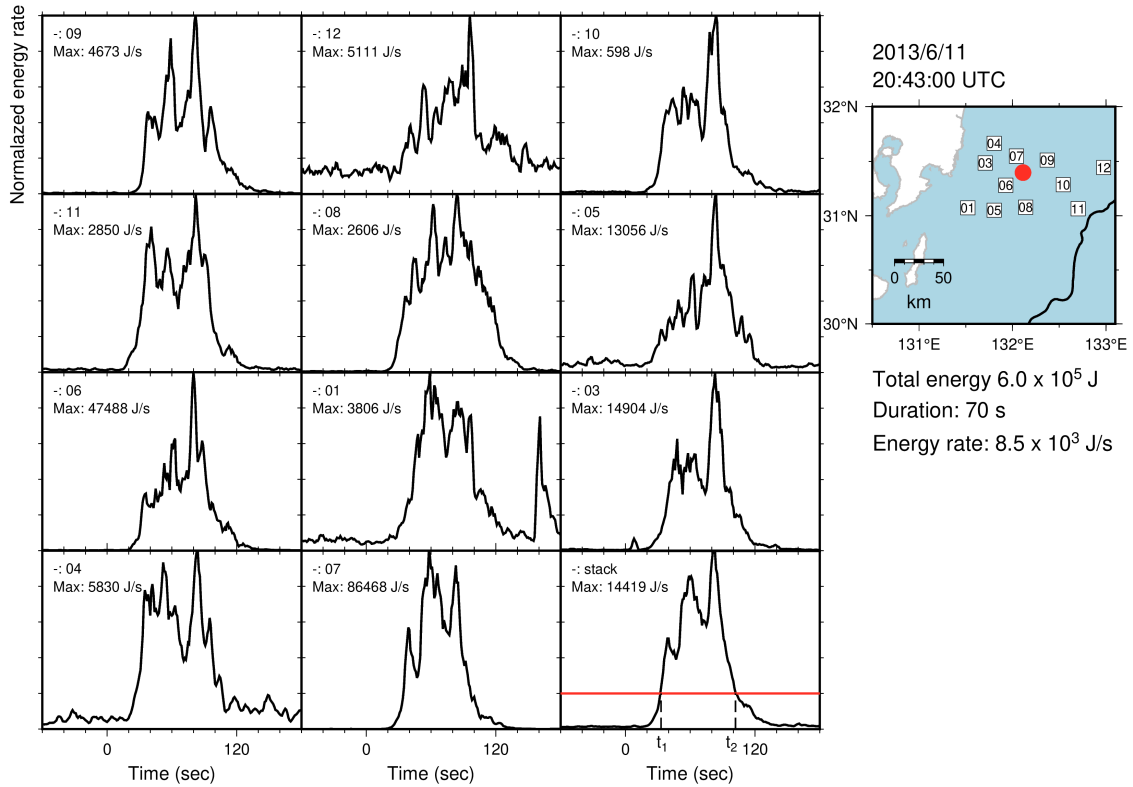
234 **Figure 4.** Site amplification factors at each OBS. Triangles represent the locations of OBSs.

235 Inverted triangle indicates the location of the reference station, N.TASF. Black line is the same as

236 displayed in Fig. 3. Estimation error of site amplification factors is shown in Fig. S2. Site

237 amplification factor at N.TASF is set as 2.0.

238



239

240

241

242

243

244

245

**Figure 5.** Temporal changes of energy rate functions of a tremor estimated at each OBS along with its stacked energy rate function. Red line of the stacked energy rate function indicates the threshold, which is set as 20% of the maximum value of the energy rate function. Red circle, squares and black line are the same as displayed in Fig. 3. Energy rate functions estimated from each station is arranged by azimuth clockwise from north.



## 246 **2.2. Estimation of moments of VLFEs**

247 We estimated the source durations and seismic moments of VLFEs temporally  
248 corresponding to the tremors in 2013 and 2015 detected by Yamashita et al. (2015; 2021)  
249 independently of tremor analysis. These values were evaluated by comparing observed and  
250 synthetic waveforms following the procedure of Yabe et al. (2021) and Baba et al. (2021). We  
251 additionally estimated the source durations and seismic moments of VLFEs in 2010 detected by  
252 Asano et al. (2015) using the same method. As long-period VLFE signals are difficult to recognize  
253 in short-period OBS records, we utilized continuous seismograms at onshore broadband F-net  
254 stations for estimation. Before the analysis, we removed the instrumental responses, resampled at  
255 one sample per second, and applied a bandpass filter in a frequency range of 0.02–0.05 Hz to  
256 enhance the VLFE signals.

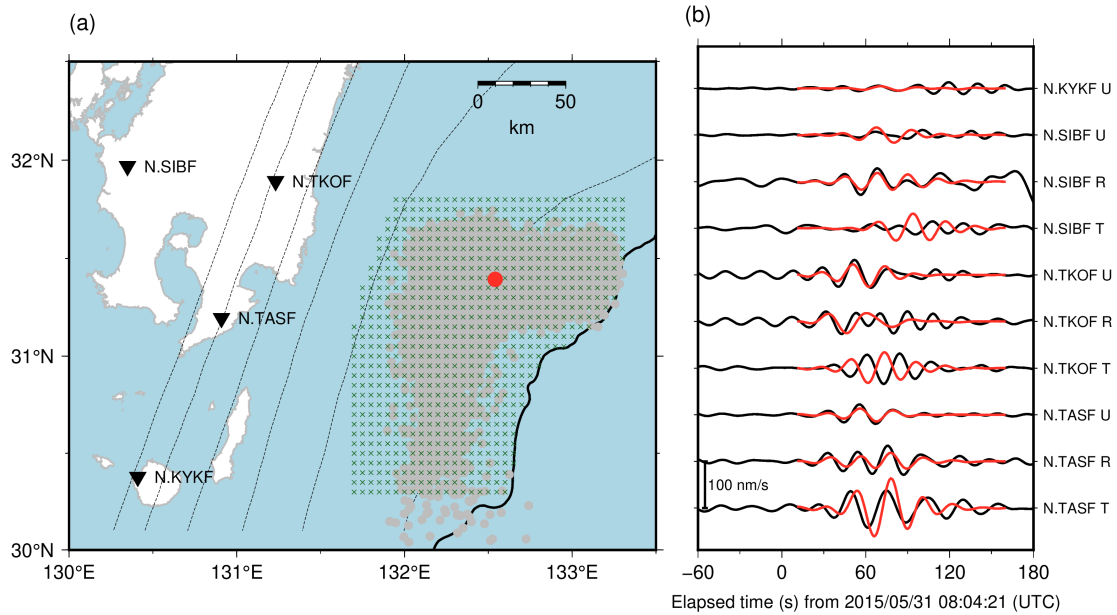
257 To reduce the computational costs of calculating Green's functions, reciprocal  
258 calculations were conducted using OpenSWPC (Maeda *et al.* 2017). We set source grids at an  
259 interval of 0.05° on the JIVSM plate boundary model of the area where tremors were detected  
260 (Fig. 6a). The hypocentre of each VLFE was assumed to be at the nearest grid from the hypocentre  
261 of the tremor located by Yamashita et al. (2015; 2021) or at the hypocentre of VLFEs located by  
262 Asano et al. (2015). To calculate Green's functions, we used a three-dimensional velocity  
263 structure model, JIVSM. For the density and quality factors, the values of JIVSM were used. A  
264 frequency-independent model was adopted when calculating Green's functions. The minimum *S*-  
265 wave velocity in the elastic volume was set as 1.5 km/s. The model includes topography  
266 (ETOPO1; Amante & Eakins 2009), air, and seawater layers. The default values of OpenSWPC  
267 were used for the density, seismic velocities, and quality factors in seawater and air. The model  
268 volume was discretized using a uniform grid of 0.2 km. The focal mechanisms were assumed to  
269 be consistent with the geometry of the plate boundary model of JIVSM and the plate convergence  
270 direction of the plate motion model NUVEL-1A (DeMets *et al.* 1994). By combining the assumed  
271 focal mechanisms and simulated Green's functions, we prepared a series of synthetic velocity  
272 seismograms with triangular functions and source durations of 10–50 s (e.g., Takemura et al.,  
273 2019).

274 We calculated the station- and component-averaged CCs between the synthetic and  
275 observed waveforms. The time window of synthetic waveform is 150 s from the assumed origin  
276 time of a VLFE. The origin time was searched for in the range from 30 s before to 30 s after the  
277 start time of the duration range of each tremor located by Yamashita et al. (2015; 2021) and the  
278 origin time of each VLFE located by Asano et al. (2015). The combination of source duration and  
279 origin time, with the highest average CC in the grid search, was adopted. The dominant range of  
280 source duration of VLFEs is 20–35 s. For tremor episodes in 2013 and 2015, if the highest  
281 averaged CC is larger than 0.3, we regard that a VLFE occurs temporally corresponding to the

282 tremor. The difference of origin times between a VLFE and the corresponding tremor is in the  
283 range of  $\pm 20$  s. For VLFE episode in 2010, events with average CCs smaller than 0.3 were  
284 discarded. We calculated the relative amplitudes by minimizing the variance reduction between  
285 observed and simulated waveforms with the source duration of the highest average CC (Baba et  
286 al. 2021; Yabe et al. 2021). We further estimated the seismic moments of VLFEs by multiplying  
287 the seismic moments of the synthetic waveform by estimated relative amplitudes. The moment,  
288 duration, and average CC of the example in Fig. 6 were  $2.0 \times 10^{15}$  Nm, 24 s, and 0.65, respectively.  
289 The seismic moment rate of the VLFE was obtained by dividing the seismic moment by the source  
290 duration which was estimated by the grid search based on CC between synthetic and observed  
291 waveforms.

292 We estimated the uncertainties of the VLFE moments by using the nonparametric  
293 bootstrap method. First, 100 bootstrap samples were prepared for each event. Since seven  
294 components are used for VLFE analysis (vertical component of N.KYKF and radial and vertical  
295 components in other F-net stations shown in Fig. 6), a bootstrap sample consisted of seven  
296 components including duplicates. Subsequently, VLFE moments were calculated by using each  
297 bootstrap sample composed of seven components. Then, we estimated the standard deviations of  
298 the 100 VLFE moments. The uncertainty of VLFE moments is 0.2–0.3 order (Fig. S3b).

299 The fit between the observed and simulated Love waves was not sufficient compared  
300 with that between observed and simulated Rayleigh wave (Fig. 6b). It may be inferred that the  
301 sedimentary structure of JIVSM at very shallow depths ( $< 5$  km) in Hyuga-nada is insufficient to  
302 simulate Love waves, which are sensitive to shallow structures. We verified that the CCs between  
303 the simulated and observed waveforms of a regular earthquake located by Takemura et al. (2020)  
304 in the transverse components were also low, whereas those in the vertical and radial components  
305 were high (Fig. S5). Therefore, we used only the vertical and radial components (Rayleigh waves)  
306 when calculating the CCs. For the N.KYKF station, only the vertical component was utilized  
307 because the horizontal components were noisy.  
308



309

310 **Figure 6.** (a) VLFE source grids for the VLFE analysis. Crosses indicate the locations of the  
 311 VLFE source grids. Gray dots indicate the epicentres of tremors detected by Yamashita et al.  
 312 (2015; 2021). Red circle indicates the epicentre of the event displayed in Fig. 6b. Dashed contours  
 313 indicate the isodepth of the top of the Philippine Sea plate at 10-km intervals (JIVSM; Koketsu  
 314 et al. 2012). Black line represents the trench axis. Inverted triangles display the locations of the  
 315 F-net stations. (b) An example of a VLFE in a frequency range of 0.02–0.05 Hz. Waveforms are  
 316 depicted from 08:04:21 (UTC), May 31, 2015. Black and red lines are the observed and the  
 317 simulated waveforms, respectively. R, T, and U components represent the radial, transverse, and  
 318 vertical components, respectively.

319

320 **3. Results**

321 We estimated the energies of 1,672 and 6,126 shallow tremors in 2013 and 2015,  
 322 respectively. We classified the analysis region into three areas based on spatial variation in  
 323 energies of tremors and moments of VLFs (Figs 7 and S6): Area A, south of 31.0° N; Area B,  
 324 west of 132.4°E, north of 31.0° N; and Area C, east of 132.4°E, north of 31.0° N (see rectangles  
 325 of Fig. 7). Area A is south of the subducted Kyushu-Palau Ridge, Area B is near the top of the  
 326 subducted ridge, and Area C is east of the subducted ridge. Most of Areas A and C are outside the  
 327 subducted ridge. In 2013, tremors and VLFs occurred mainly in Areas A and B, whereas in 2015,  
 328 they occurred mainly in Areas B and C. The dominant range of tremor energies was  $10^{3.5}$ – $10^{7.5}$  J  
 329 with spatial variation (Fig. 7ac). In 2013 (Fig. 7a), tremors with higher energies ( $> 10^6$  J) were  
 330 concentrated in Area A. This characteristic is confirmed in the maximum and median values of  
 331 tremor energies (Fig. S6a). In 2015 (Fig. 7c), tremors with higher energies ( $> 10^{6.5}$  J) occurred  
 332 near the north-eastern edge of the subducted Kyushu-Palau Ridge in Area C. The tremor energies  
 333 near the trench axis in Area C were lower. These characteristics are also shown in the maximum  
 334 tremor energies (Fig. S6b). Although median tremor energies are low in the longitude of 132.5°–  
 335 132.7° due to the detection of many small events, the north-eastern edge of the subducted Kyushu-  
 336 Palau Ridge in Area C is considered as high tremor energy area.

337 The moments were also estimated for 1,297, 904, and 1,785 shallow VLFs in 2010,  
 338 2013, and 2015, respectively. The dominant range of the VLF moments was  $10^{13.5}$ – $10^{16.5}$  Nm  
 339 (Fig. 7b, d,e, and f). South of 31.0° N (Area A), VLFs with higher moments ( $> 10^{15.5}$  Nm)  
 340 occurred in 2010 and 2013 (Fig. 7be). North of 31.0° N, VLFs extended near the trench axis in  
 341 2010 and 2015. In particular, VLFs with higher moments ( $> 10^{15.5}$  Nm) in 2010 and 2015 (Figs  
 342 7de) are concentrated in Area C. In Area B, the VLF moments are relatively low. These  
 343 observations are stably confirmed in the maximum and median values of VLF moments (Fig.  
 344 S6c-f). The spatial variations in the VLF moments and tremor energies for each observation  
 345 period were similar (Fig. 7). The change in the maximum range of tremor energy or VLF  
 346 moment between Areas A and C and Area B is approximately one order (Fig. 7). Considering the  
 347 uncertainty of tremor energies (0.5–1orders) and VLF moments (0.2–0.3 orders), the spatial  
 348 variation in tremor energy and VLF moment is considered to be real. The spatial variations in  
 349 the energy rates of tremors and moment rates of VLFs were also approximately one order higher  
 350 in Areas A and C than in Area B (Fig. S7). We summarized our observations: the energies of the  
 351 tremors and moments of VLFs are generally higher outside the subducted ridge (Areas A and C)  
 352 than near the top of the subducted ridge (Area B).

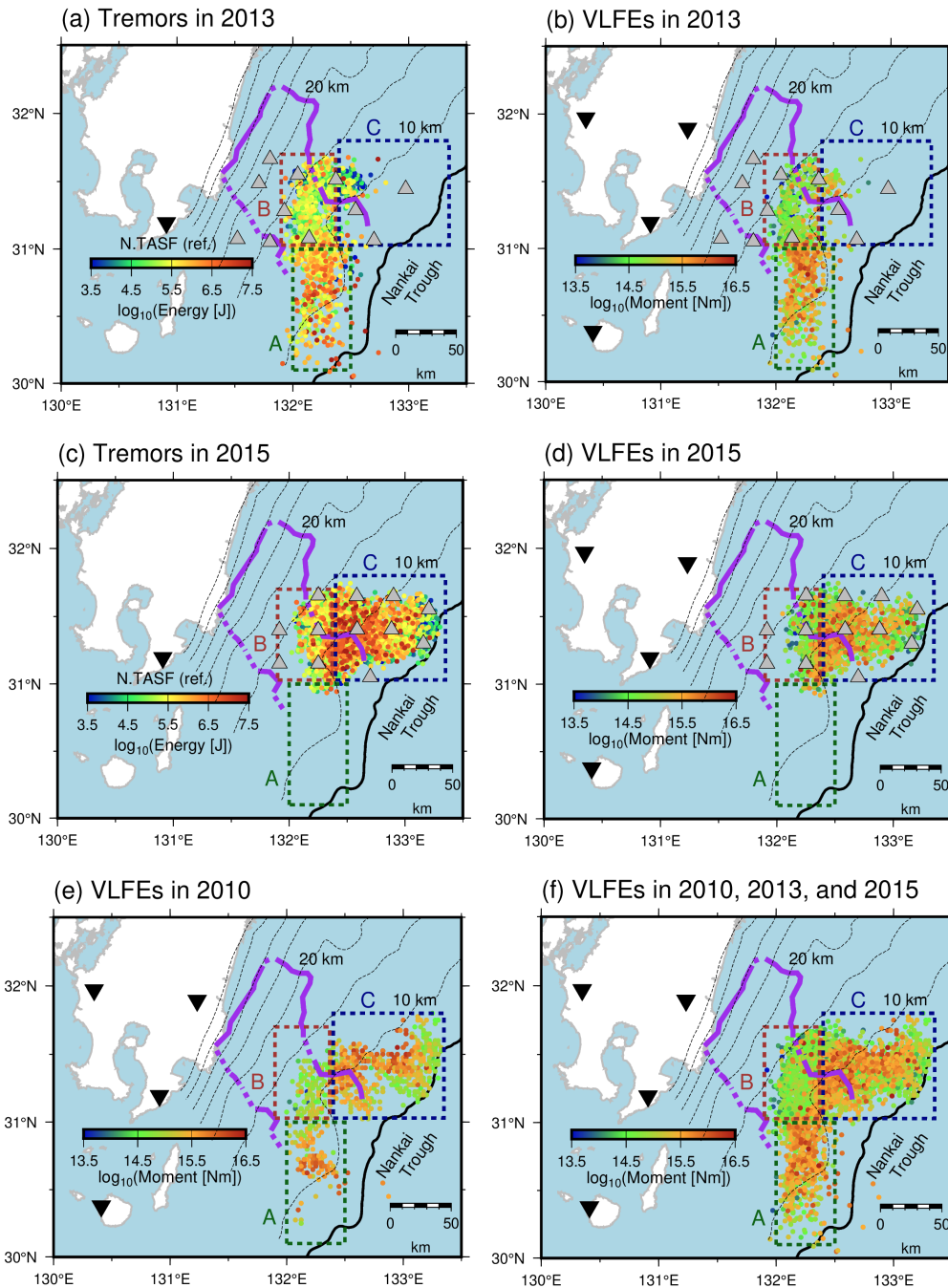
353 The spatiotemporal variation in moments and energies of slow earthquakes and the  
 354 change in the migration speed are associated (Fig. 8a and b). Hereafter, we mainly discuss the  
 355 spatiotemporal variation in slow earthquakes based on VLF activity because the spatiotemporal

356 variations in VLFE moments and tremor energies were similar, and the VLFE analysis covered  
357 all episodes in 2010, 2013, and 2015. Here, we summarized migration patterns in each episode.  
358 Their detailed features were described in the previous studies (Asano et al. 2015; Yamashita et al.  
359 2015; Yamashita et al. 2021). The episodes in 2010 and 2015 are divided into three migrations  
360 and the 2013 episode is divided into two migrations (Figs. S8–S15 and Table S1). The 2010a,  
361 2013a, and 2013b migrations were northward along the strike, whereas the 2010b, 2010c, 2015a,  
362 2015b, and 2015c migrations were along the dip with various directions (Figs 8 and S8–S15;  
363 Table S1). All migrations along the strike direction consistently started in Area A (Figs 8b, S8,  
364 S11, and S12). Subsequently, the VLFES migrated northward and entered the subducted ridge.  
365 After VLFES entered Area B, their migration speed became slow (Fig. 8a and b). The  
366 spatiotemporal variation in the migration front seems to be parabolic (discussed in detail in  
367 Section 4.1). Rapid tremor reversals (RTRs; red dotted arrows in Figs 8b and S11), which is a fast  
368 backward migration (e.g., Houston et al. 2011), occurred during the migration in 2013.

369 In the main front of along-strike migrations, the moments of VLFES became lower and  
370 the migration speed slowed after the front entered the Area B (Figs 8b, S8, S11, and S12).  
371 Therefore, the migration speed and the moments of VLFES are positively correlated. On the other  
372 hand, the moments of the VLFES in RTRs became higher when RTRs entered Area A (Figs 8b  
373 and S11). This suggests that the moments of VLFES depend on the location.

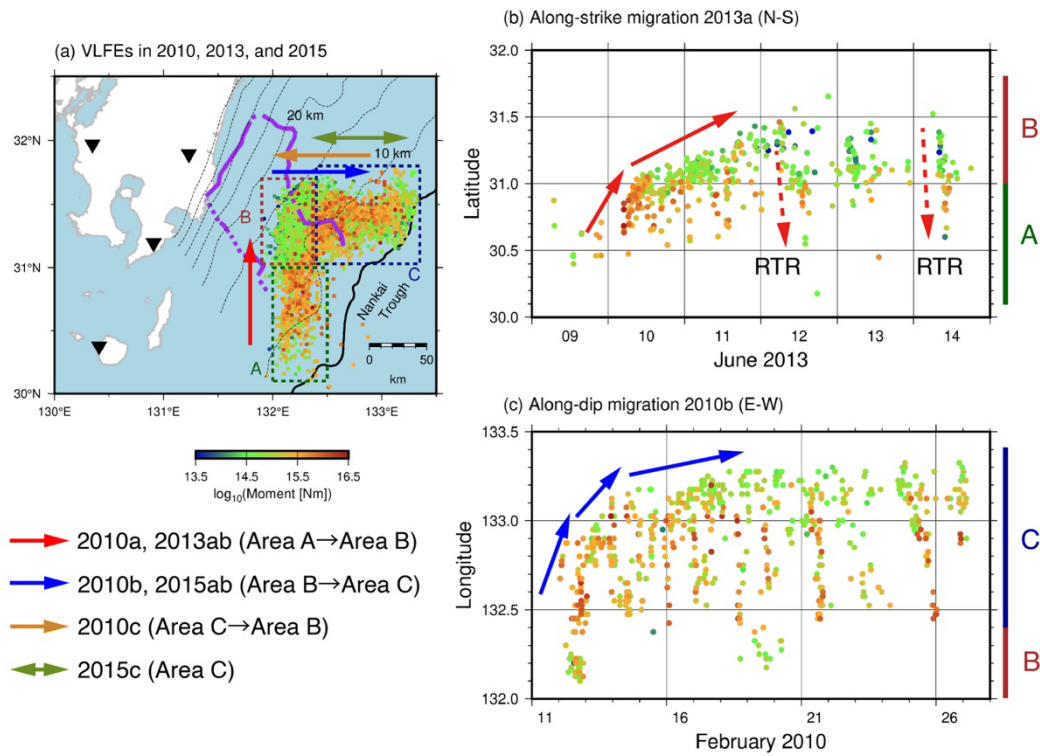
374 In the downdip of shallow tremors and VLFES, repeating earthquakes occurred at depths  
375 of 15–30 km (Fig. 9). The repeating earthquake activity manifests that the plate boundary around  
376 its patch is creeping; therefore, the large slip rate by repeating earthquakes suggests that the  
377 interplate coupling is weak (e.g., Uchida & Matsuzawa 2011). Fig. 9 compares the spatial  
378 distributions of slip rates from repeating earthquakes and cumulative moments of VLFES.  
379 Cumulative moments of VLFES may be also linked with the strength of interplate coupling (Baba  
380 *et al.* 2020). The interplate slip rate estimated from repeating earthquakes was higher in the south  
381 along the strike direction (Yamashita et al. 2012); therefore, the interplate coupling may be weaker  
382 at depths of 15–30 km in the south (downdip part of Area A) than in the north (downdip of Area  
383 B). The cumulative moment of shallow VLFES in 2010 and 2013, episodes with along-strike  
384 migrations, was also lower in Area B than in Area A during the episodes (Fig. 9). Baba et al.  
385 (2020) found the tendency that cumulative moment of shallow VLFES was higher in areas with  
386 weak interplate coupling along the Nankai Trough. In Hyuga-nada, the slip rate of repeating  
387 earthquakes and the cumulative moment of VLFES are higher in the south (in and downdip of  
388 Area A) than in the north (in and downdip of Area B). These observations suggest that although  
389 there is a difference in the slip behaviour along the dip direction, such as repeating earthquakes  
390 and VLFES, the interplate coupling may be consistently weak in the south along the strike  
391 direction. Although Area C is the northern part of Hyuga-nada, the cumulative moment of VLFES

392 is high. Area C is apart from the repeating earthquake area and close to the trench axis unlike  
 393 Areas A and B; therefore, interplate coupling may be different from Area B.  
 394

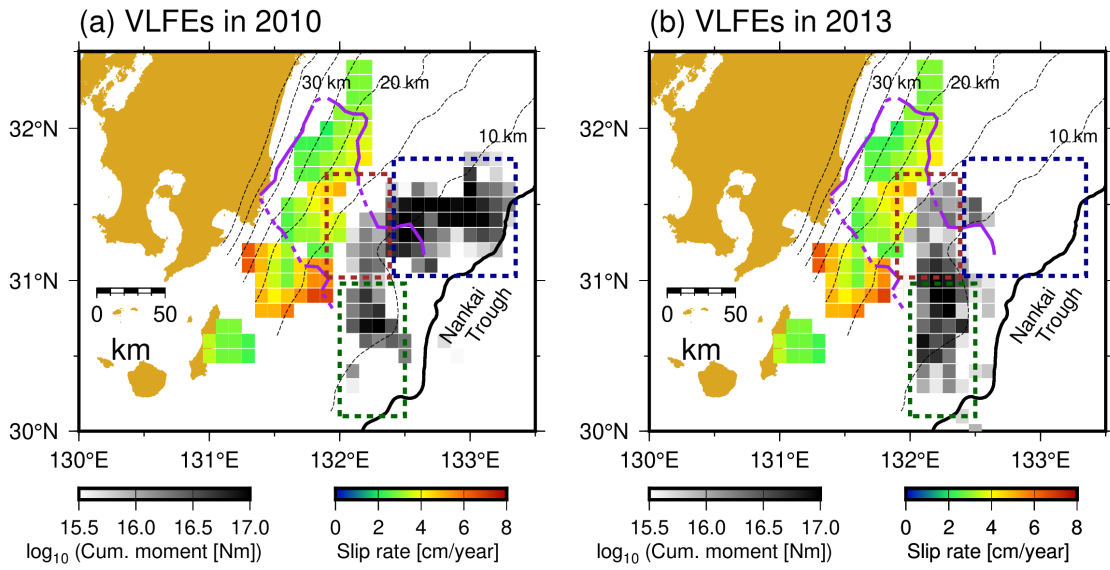


395  
 396 **Figure 7.** Spatial distribution of (a) energies of tremors in 2013, (b) moments of VLFs in 2013,  
 397 (c) energies of tremors in 2015, (d) moments of VLFs in 2015, (e) moments of VLFs in 2010,  
 398 and (f) moments of VLFs in all analysis periods. Green, brown, and dark blue dotted rectangles  
 399 indicate the ranges of Area A, B, and C, respectively. Purple lines represent the inferred subducted

400 Kyushu-Palau Ridge (Yamamoto *et al.* 2013). Gray triangles depict the locations of OBSs. Black  
 401 line represents the trench axis. Inverted triangles display the locations of the F-net stations.  
 402 Dashed contours indicate the isodepth at the top of the Philippine Sea plate in intervals of 5 km  
 403 (Nakanishi *et al.* 2018).  
 404



405  
 406 **Figure 8.** (a) Summary of slow earthquake migration patterns. Coloured arrows represent the  
 407 direction of migration patterns. Coloured dotted rectangles, dashed contours, purple lines and  
 408 black inverted triangles are the same as displayed in Fig. 7. (b and c) Spatiotemporal distributions  
 409 of (b) the along-strike migration 2013a and (c) the along-dip migration 2010b with moments of  
 410 VLFEs. Coloured arrows indicate the direction of migrations. Red dotted arrows in Fig. 8b  
 411 represents the RTR.  
 412  
 413



414

415 **Figure 9.** Relationship between slip rates estimated from repeating earthquakes (Yamashita et al.  
416 2012) and shallow slow earthquakes. Gray scales exhibit the cumulative moments of VLFs.  
417 Colour scale indicates the slip rate estimated from repeating earthquakes. Coloured dotted  
418 rectangles, purple lines, black lines, and dashed contours are the same as in Fig. 7.

419

420



## 421 **4. Discussion**

### 422 **4.1. Along-strike spatial variation in slow earthquake activity**

423 To investigate the controlling factor of the along-strike variation in slow earthquake  
424 activity in Hyuga-nada, we compared the activity with a physical model of along-strike slow  
425 earthquake migration by Ando et al. (2012). In their model, high- and low-strength brittle tremor  
426 patches exist on the ductile background based on Newtonian rheology. The rupture of these brittle  
427 patches is triggered by the stress increase at the migration front of an SSE. They predicted that  
428 tremors start migrating energetically in areas with high tremor-patch strength (strong patch areas)  
429 and decelerates with a parabolic spatiotemporal pattern in areas with low tremor-patch strength  
430 (weak patch areas). In Hyuga-nada, the migration speed was faster, and the VLFE moment was  
431 higher in Area A than in Area B (Fig. 8). These observations are consistent with the modelling  
432 results by Ando et al. (2012). The along-strike variation in slow earthquake activity in Hyuga-  
433 nada can be explained by the difference in the patch strength of slow earthquakes, where Areas A  
434 and B are considered strong and weak patch areas, respectively (Fig. 10).

435 The spatial variations in tremor activity in Shikoku and VLFE activity off the south-  
436 eastern Kii Peninsula were also discussed based on Ando et al. (2012) (Shikoku: Kano et al.  
437 2018b; off the southeast Kii Peninsula: Yamamoto et al. 2022). In Shikoku, western and central  
438 Shikoku were interpreted as strong and weak patch areas, respectively, whereas the areas west of  
439 and inside the subducted Paleo-Zenisu ridge off the Kii Peninsula were regarded as strong and  
440 weak patch areas, respectively.

441 A possible factor for the along-strike spatial variation in slow earthquake activity in  
442 Hyuga-nada is the spatial heterogeneity of pore fluid pressure. Kano et al. (2018b) suggested that  
443 the heterogeneity of strong and weak patch areas is caused by the variation in effective normal  
444 stress, which is associated with that in the fluid pressure on the plate boundary. Takemura et al.  
445 (2022a) discussed that the variation in the pore fluid pressure can induce the change of the  
446 migration speed, which can be considered as a proxy for rupture propagation of an SSE (e.g.,  
447 Bartlow et al. 2011; Ito et al. 2007), off the Cape Muroto and Kii Peninsula. In Hyuga-nada, the  
448 change in migration speed between Area A and B may be caused by the pore fluid pressure  
449 heterogeneity. To discuss the variation in the pore fluid pressure in Hyuga-nada in more detail,  
450 investigations of seismic velocity structures (especially  $V_S$  and  $V_p/V_S$  ratio) are required in future  
451 work.

452 Another possible factor is the geometrical effects of the subduction of a ridge. Wang  
453 and Bilek (2011) suggested that a fracture network caused by a subducted seamount generates  
454 structural and stress heterogeneities. According to Chesley et al. (2021), the subduction of a  
455 seamount can transport a considerable volume of fluid to the forearc and create a fluid-rich  
456 fracture zone, which can change the effective normal stress around the plate boundary. Takemura

457 et al. (2022b) and Yamamoto et al. (2022) suggested the variation in cumulative moments of  
 458 VLFs which is associated with subducted Paleo-Zenisu ridge off the Kii Peninsula. In Hyuga-  
 459 nada, the subduction of the Kyushu-Palau ridge may also generate the stress heterogeneity on the  
 460 plate boundary.

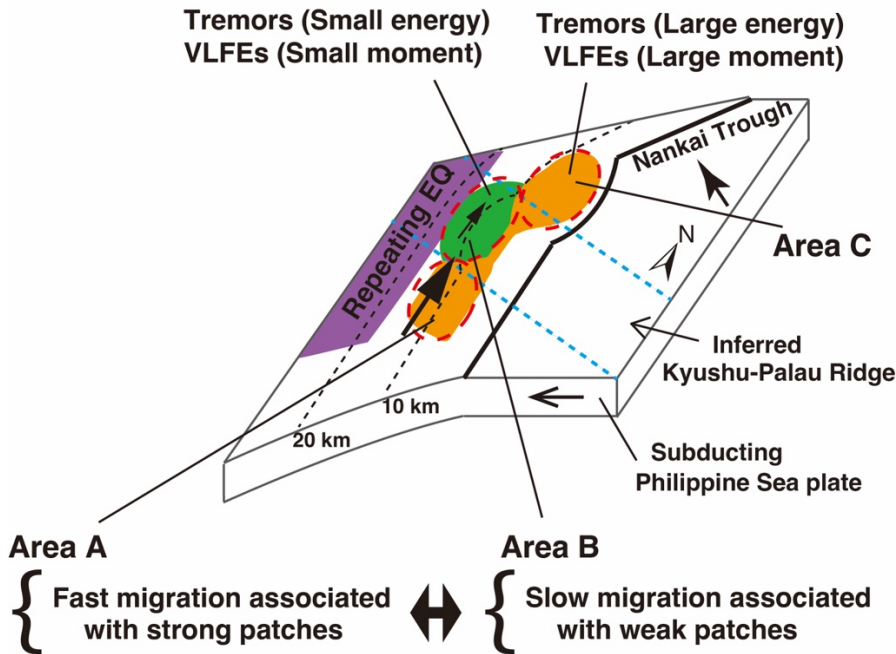
461 As mentioned in Section 3, the spatiotemporal variation in the migration front appears  
 462 to be parabolic. Following Ando et al. (2012), we investigated which function is better for fitting  
 463 the migration front in 2013a, exponential ( $t = C \exp(a(x + x_1)) + t_1$ ;  $t$  is the elapsed time,  $x$  is  
 464 the migration distance,  $C$ ,  $a$ ,  $x_1$ , and  $t_1$  are constant) or parabolic ( $t = D^{-1}(x + x_2)^2 + t_2$ ;  $D$  is  
 465 the diffusion coefficient,  $x_2$  and  $t_2$  are constant). Although tremor epicentres were scattered around  
 466 the start of migration, the migration pattern seems to be better fitted by a parabola (Fig. 11) rather  
 467 than exponential, and the diffusion coefficient  $D$  is evaluated as  $\sim 6 \times 10^4 \text{ m}^2/\text{s}$  (Fig. S16).

468 Ando et al. (2012) assumed that fault strength is equals to  $\tau_p$  when slip velocity  $v=0$  and  
 469 equals to  $\tau_r + \eta v$  when  $v > 0$  following Ando et al. (2010) and Nakata et al. (2011).  $\tau_p$ ,  $\tau_r$ ,  $\eta$  are peak  
 470 strength, residual strength, and viscosity factor, respectively. In Ando et al. (2012),  $\tau_r$  is set as zero  
 471 and the patch strength is represented by  $\tau_p$ . The difference in  $\tau_p$  between strong and weak patches  
 472 is supposed to be represented by that in stress drop. Therefore, we roughly evaluated the variation  
 473 in the stress drop of the VLFs in Hyuga-nada. Assuming a circular crack model, the seismic  
 474 moment  $M_0$  of an earthquake is given by (e.g., Kanamori & Anderson 1975):

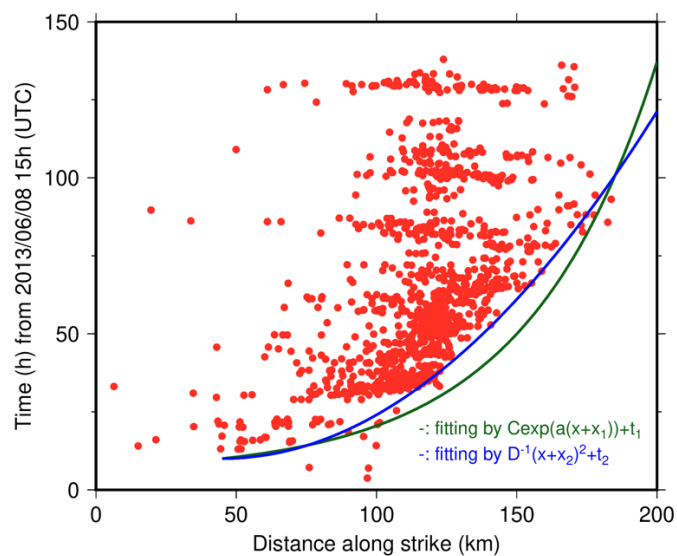
$$475 \quad M_0 = \frac{16}{7} \Delta \tau r^3 \quad (5)$$

476 where  $\Delta \tau$  is the stress drop and  $r$  is the radius of the patch. In this section, this relationship is  
 477 further assumed in VLFs. The median moment of a VLFE in Area A (strong patch area) and in  
 478 Area B (weak patch area) is  $(2.2 \pm 1.2) \times 10^{15} \text{ Nm}$  and  $(6.5 \pm 4.1) \times 10^{14} \text{ Nm}$ , respectively (Fig. 7b, d,  
 479 e, and f). Considering that Ohta & Ide (2017) estimated the source radius of a deep VLFE with  
 480  $M_0 = 1.2 \times 10^{14} \text{ Nm}$  as  $\sim 5 \text{ km}$ , we assume the radius of a shallow VLFE patch in Hyuga-nada with  
 481  $M_0 = 10^{13.5} - 10^{16.5} \text{ Nm}$  (Figs. 7b, d, e, f, S6c, and S6e) as 3–30 km. If patches with a radius  $r$  of 3–  
 482 30 km are assumed, the median stress drop of a VLFE in Areas A and B is evaluated as  $3.6 \times 10^1 -$   
 483  $3.6 \times 10^4 \text{ Pa}$  and  $1.1 \times 10^1 - 1.1 \times 10^4 \text{ Pa}$ , respectively. The spatiotemporal distribution of migration is  
 484 parabolic if the difference in stress drop between strong and weak patches is sufficient (Ando et  
 485 al. 2012). As indicated by the fitting of the migration front, the spatiotemporal variation in the  
 486 slow earthquake migration front was parabolic (Figs. 8b and 11). Although the model of Ando et  
 487 al. (2012) assumed an 11-times differences between strong and weak patches, if the patch size in  
 488 Areas A and B is similar, parabolic migration pattern was observed by an approximately three-  
 489 time difference in the stress drops of these patches in Hyuga-nada. On the other hand, since the  
 490 difference in the moment of VLFs between Areas A and B may be due to the patch size, slip  
 491 distribution of VLFs should be investigated in future studies. However, the estimation of slip

492 areas of shallow VLFs is a challenging issue due to offshore heterogeneities along the  
 493 propagation path. The patch heterogeneity may be a key factor of variations in tremor energy,  
 494 VLFs moment, and migration speed in Hyuga-nada. Although we conducted a general  
 495 classification of slow earthquake areas, more statistical approaches, such as clustering procedures,  
 496 may be useful to construct a new model of slow earthquake activity.  
 497



498  
 499 **Figure 10.** Schematic illustration of the interpretation of distributions of slow earthquakes and  
 500 Kyushu-Palau Ridge.  
 501  
 502  
 503  
 504



505

506 **Figure 11.** Spatiotemporal distribution of tremor migration in the episode of 2013a. Vertical and  
507 horizontal axis shows the elapsed time from 2013/06/08 15:00:00 (UTC) and distance along the  
508 strike (N-S) from 30.0°N, respectively. Blue and green lines indicate the parabolic and exponential  
509 curves, respectively.

510

511 **4.2. Scaled energy of shallow slow earthquakes in Hyuga-nada**

512 To discuss the characteristics of the source process of slow earthquakes in Hyuga-nada,  
 513 we estimated the scaled energy following previous studies (e.g., Ide et al., 2008; Yabe et al., 2019;  
 514 2021) using the ratio between the tremor energy rate and VLFE moment rate for activities in 2013  
 515 and 2015, when the energy rate could be estimated from the OBS records. The dominant range of  
 516 the scaled energy was  $10^{-11.5}$ – $10^{-8.5}$  both in 2013 and 2015 (Fig. 12ab). Dominant ranges of scaled  
 517 energies did not change significantly between episodes in 2013 and 2015 (Fig. S17). The range  
 518 of the median scaled energy is in the range of  $10^{-10.5}$ – $10^{-9.5}$  in all areas (Fig. 12cd). The median  
 519 scaled energy is approximately 0.5 orders smaller around the eastern edge of the Kyushu-Palau  
 520 Ridge in Area C than in other areas. However, the variation in scaled energy is ranged to three to  
 521 four orders in all areas (Fig. S17). In addition, the uncertainty of scaled energy often reaches  
 522 approximately one order (Fig. S18). Therefore, it is difficult to consider that the 0.5 orders  
 523 difference in median scaled energy in the western part of Area C is due to the variation in the  
 524 rupture process in Hyuga-nada. The characteristics of the scaled energy do not change in spatially  
 525 and temporally in the order scale inside the Hyuga-nada. Apparent stress is estimated by  
 526 multiplying scaled energy by rigidity. Since the range of scaled energy is similar between Areas  
 527 A and B, the apparent stress is similar if the rigidity is the same.

528 The range of scaled energies in Hyuga-nada is similar to or one order smaller compared  
 529 to the off the Cape Muroto and Kii Peninsula ( $10^{-10}$ – $10^{-8}$ ; Yabe et al. 2021, 2019), along the Japan  
 530 Trench ( $10^{-10}$ – $10^{-9}$ ; Yabe et al. 2021), and in Costa Rica ( $10^{-9}$ – $10^{-8}$ ; Baba et al. 2021). The range  
 531 of scaled energies of shallow slow earthquakes in Hyuga-nada is also similar to those of deep  
 532 slow earthquakes in southwest Japan, Cascadia, and Mexico ( $10^{-9.5}$ – $10^{-9}$ ; Ide, 2016; Ide and Maury,  
 533 2018; Ide and Yabe, 2014; Fig. 13). However, the range of scaled energy in Hyuga-nada is broader  
 534 than other slow earthquake regions.

535 Ide (2008) and Ide & Maury (2018) discussed the theoretical relationship between  
 536 seismic energy rate and seismic moment rate of slow earthquakes by the Brownian slow  
 537 earthquake model. In their model, the characteristic size of the slip area  $S$  is described by:

538 
$$S = Cr^2 \quad (6)$$

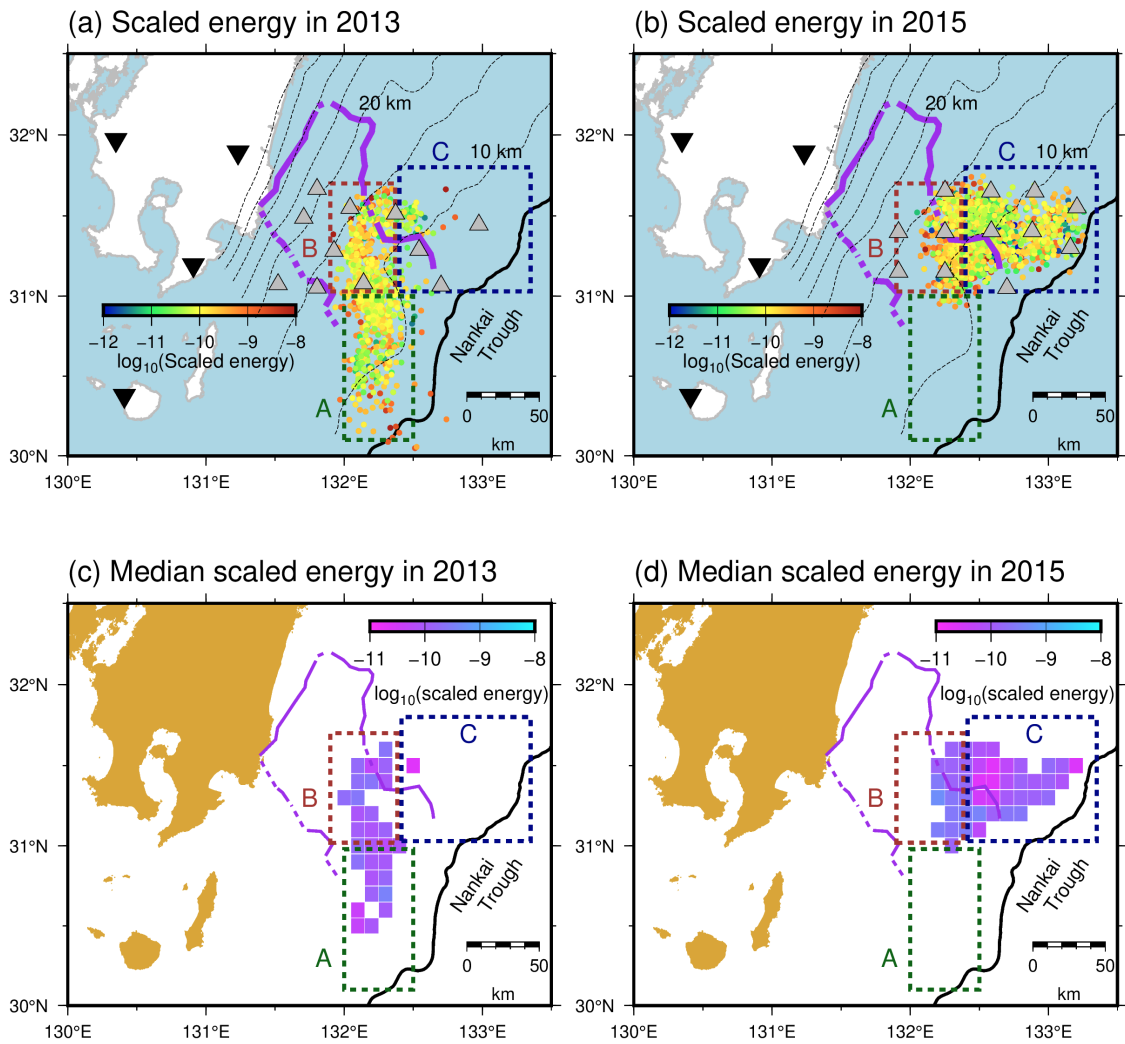
539 where  $r$  is a random variable and  $C$  is a constant. The temporal change of  $r$  is described by:

540 
$$dr = -\alpha r dt + \sigma dB \quad (7)$$

541 where  $\alpha$  is the characteristic frequency of slow earthquakes ( $\alpha^{-1}$  is a characteristic time),  $dB$  is the  
 542 random variable of Gaussian distribution with the mean 0 and the variance 1,  $\sigma$  is the fluctuation  
 543 magnitude. They discussed that the energy rate divided by the square of the moment rate depends  
 544 on a characteristic frequency of a slow earthquake event,  $\alpha$ :

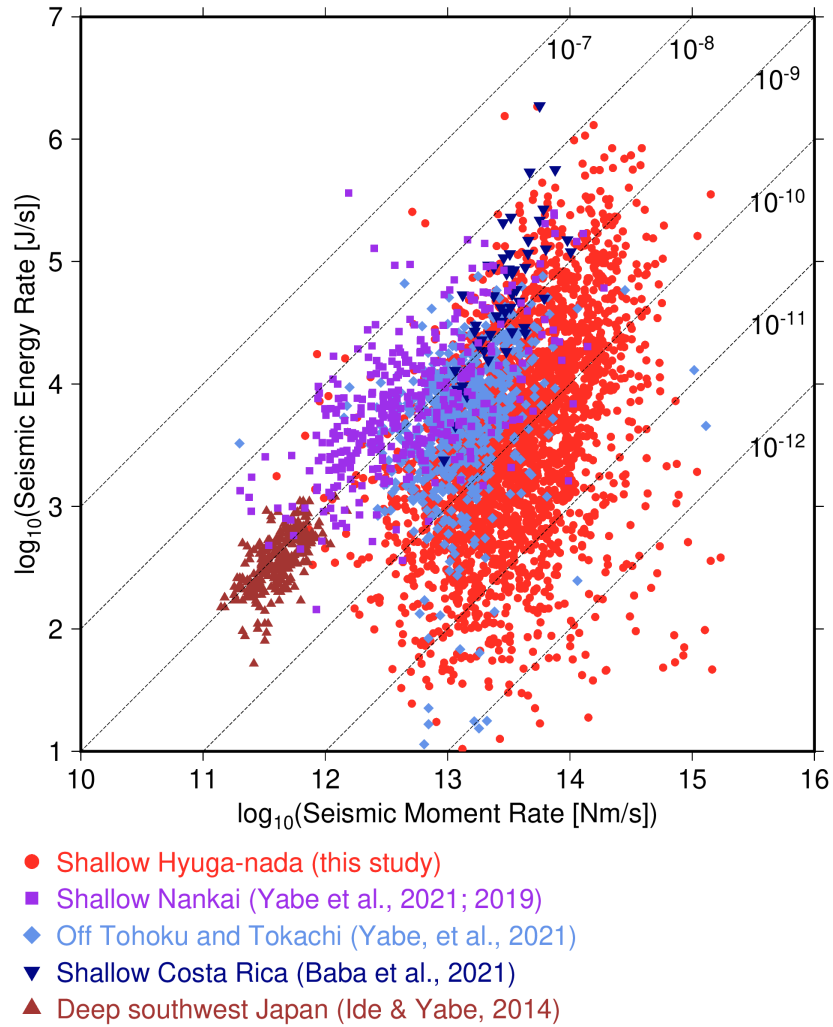
545 
$$\frac{E[Er_{rate}]}{E[Mr_{rate}]^2} = \frac{4\alpha}{5\pi\rho V_s^5 \Delta t} \quad (8)$$

546 where  $\rho$  is the density,  $V_s$  is the  $S$ -wave velocity, and  $\Delta t$  is the time steps of the stochastic process.  
547  $E[E_{rate}]$  and  $E[M_{rate}]$  indicates the long-term averages of energy rates and moment rates,  
548 respectively. Ide & Maury (2018) evaluated  $E[E_{rate}]/E[M_{rate}]^2$  and  $\alpha^{-1}$  of seismic slow earthquakes  
549 in deep southwest Japan, Cascadia, and Mexico as  $10^{-22}$ – $10^{-20}$  and 0.3–30 s, respectively. The  
550 range of  $\alpha^{-1}$  of the SSE scale in deep southwest Japan, Cascadia, and Mexico evaluated by Ide &  
551 Maury (2018) is 75–300 s.  $E[E_{rate}]/E[M_{rate}]^2$  in Hyuga-nada is estimated to be  $10^{-25}$ – $10^{-21.5}$  (Fig.  
552 S19). The small value of  $E[E_{rate}]/E[M_{rate}]^2$  may be caused by small  $\rho$  and/or  $V_s$  in Hyuga-nada.  
553 However, if  $\rho$ ,  $V_s$ , and  $\Delta t$  is the same order as in the values of Ide & Maury (2018),  $\alpha^{-1}$  in Hyuga-  
554 nada is estimated to be 10–30000 s. In Hyuga-nada, there may be slow earthquake events that  
555 have similar or longer characteristic times than those of other slow earthquake regions. In addition,  
556 the range of the characteristic time is broader in Hyuga-nada than in other slow earthquake  
557 regions; therefore, slow earthquakes in Hyuga-nada may have various spectral features. Based on  
558 Ide & Maury (2018), the wide range of characteristic time in this area suggests width variations  
559 of tremor source area.  
560  
561



562

563 **Figure 12.** Spatial distribution of scaled energy of shallow slow earthquakes (a) in 2013 and (b)  
 564 in 2015. Spatial distribution of the median scaled energy in the grid of  $0.1^\circ \times 0.1^\circ$  where the  
 565 number of events is larger than 10 (c) in 2013 and (d) in 2015. Coloured dotted rectangles, purple  
 566 lines, black lines, gray triangles, inverted triangles, and dashed contours are the same as in Fig. 7.  
 567



568

569 **Figure 13.** Relationship between seismic moment rates of VLFs and seismic energy rates of  
570 tremors. Red circles, purple squares, green diamonds, dark blue inverted triangles, and dark blue  
571 triangles indicate the relationships between seismic moment rates of VLFs and seismic moment  
572 rates of tremors in shallow Hyuga-nada (this study), shallow Nankai except Hyuga-nada (Yabe *et*  
573 *al.* 2019, 2021), off Tohoku and Tokachi (Yabe *et al.* 2021), shallow Costa Rica (Baba *et al.* 2021),  
574 and deep slow earthquakes (Ide & Yabe 2014; Ide 2016; Ide & Maury 2018). Dashed lines  
575 represent scaled energies of  $10^{-7}$ ,  $10^{-8}$ ,  $10^{-9}$ ,  $10^{-10}$ ,  $10^{-11}$ , and  $10^{-12}$ .

576

577



578 **5. Conclusion**

579 To investigate the spatial variation in the source characteristics of shallow slow  
580 earthquakes in Hyuga-nada at a higher resolution, we estimated the energies of shallow tremors,  
581 moments of shallow VLFs, and the scaled energy of shallow slow earthquakes in Hyuga-nada  
582 using the data from permanent onshore broadband and temporary offshore seismometers. The  
583 dominant ranges of energies of tremors and moments of VLFs are  $10^{3.5}$ – $10^{7.5}$  J and  $10^{13.5}$ – $10^{16.5}$   
584 Nm, respectively. The energies of tremors and moments of VLFs are higher in Areas A and C  
585 (most of which are outside the subducted Kyushu-Palau Ridge) than in Area B (near the top of  
586 the subducted ridge). The migration of tremors and VLFs along the strike direction started in  
587 Area A (south of the subducted ridge) with events of higher tremor energies and VLF moments.  
588 After going north and entering Area B (near the top of the subducted ridge), the migration speed  
589 slowed, and the tremor energies and VLF moments were observed to be low (Fig. 8b).

590 Based on the physical model of Ando et al. (2012), strengths of slow earthquake  
591 patches in Areas A and B are expected to be strong and weak, respectively. The spatiotemporal  
592 distribution of the tremor migration in 2013 is fitted by a parabolic function with the high energy  
593 and moment events at the initiation of the migration in Area A. If a circular crack model and same  
594 patch sizes are assumed, the difference in median stress drop of the VLFs in Area A (strong  
595 patch) and Area B (weak patch) is evaluated as three times. This difference in the stress drop of  
596 strong and weak patches may generate a parabolic migration pattern. The along-strike variation  
597 in the rupture process on the plate boundary, such as the stress drop, in slow earthquake regions  
598 can cause variations in the moment of slow earthquakes and migration pattern near the southern  
599 edge of the subducted ridge.

600 The dominant range of scaled energy of slow earthquakes in Hyuga-nada is estimated  
601 as  $10^{-11.5}$ – $10^{-8.5}$ . The range of scaled energies in Hyuga-nada is similar to or one order smaller than  
602 other slow earthquake regions. Inside the Hyuga-nada, the spatial variation in scaled energy is not  
603 found. Since the range of scaled energy is similar between Areas A and B, the apparent stress may  
604 be similar if the rigidity is the same. Furthermore, this range is broader than other regions. Based  
605 on the Brownian slow earthquake model by Ide & Maury (2018), the characteristic times of slow  
606 earthquakes in Hyuga-nada (10–30000 s) is similar to or longer than those of other slow  
607 earthquake regions (0.3–30 s). Following Ide & Maury (2018), the wide range of characteristic  
608 time suggests the width variations of slow earthquake source area in Hyuga-nada. The slow  
609 earthquakes in Hyuga-nada may have various spectral features.

610

611

612 **Acknowledgements**

613 We would like to thank the Editor Víctor M. Cruz-Atienza, the Assistant Editor Louise  
614 Alexander, and two anonymous reviewers for their valuable comments and suggestions. We thank  
615 Ryosuke Ando, Aitaro Kato, Satoshi Ide, Asuka Yamaguchi, Shoichi Yoshioka, Takashi Tonegawa,  
616 Ryuta Arai, Masaru Nakano, Takane Hori, Eiichiro Araki, and Yojiro Yamamoto for their valuable  
617 discussions. We appreciate Youichi Asano for providing the shallow VLFE data in 2010. This  
618 research was supported by the JSPS KAKENHI Grant in Science Research on Innovative Areas  
619 “Science of Slow Earthquakes” (JP16H06472), Grant-in-Aid for Scientific Research on  
620 Transformative Research Areas (A) “Science of Slow-to-Fast earthquakes” (JP21H05205), and  
621 JSPS Research Fellowship DC1 (JP19J20760). This study was also supported by the ERI JURP  
622 2021-S-B102. This research is part of Satoru Baba’s PhD thesis (Baba, 2022).

623

624 **Author contribution statement**

625 SB conducted analysis and drafted the manuscript. SB, ST, KO, TA, YY, and MS  
626 contributed the interpretation of this study. YY and MS designed the ocean bottom seismometer  
627 observation. All authors read and approved the manuscript.

628

629 **Data availability statement**

630 A part of OBS data for this study was acquired by “Research project for compound  
631 disaster mitigation on the great earthquakes and tsunamis around the Nankai Trough region,” a  
632 project of the Ministry of Education, Culture, Sports, Science and Technology, Japan. The OBS  
633 data is available from the corresponding author upon request. We used the F-net broadband  
634 seismograms from the National Research Institute for Earth and Disaster Resilience (2019) and  
635 the earthquake catalogues from the Japan Meteorological Agency  
636 ([https://www.data.jma.go.jp/svd/eqev/data/bulletin/index\\_e.html](https://www.data.jma.go.jp/svd/eqev/data/bulletin/index_e.html)). OpenSWPC code Version  
637 5.0.2 (Maeda *et al.* 2017) was utilized to calculate synthetic waveforms. We used the Fujitsu  
638 PRIMERGY CX600M1/CX1640M1 (Oakforest-PACS) at the Information Technology Center,  
639 the University of Tokyo for numerical simulations. Generic mapping tools (Wessel *et al.* 2013)  
640 and the Seismic Analysis Code (Helfrich *et al.*, 2013) are used to prepare figures and process  
641 seismograms, respectively. Catalogues of shallow tremors detected by Yamashita *et al.* (2015;  
642 2021) can be downloaded from the Slow Earthquake Database (Kano, *et al.* 2018a). The estimated  
643 tremor energies and VLFE moments are provided in an open access repository, zenodo  
644 (<https://doi.org/10.5281/zenodo.8220097>).

645

646

647

648 **References**

- 649 Amante, C., & Eakins, B.W. 2009. ETOPO1 1 Arc-Minute Global Relief Model: Procedures, Data  
650 Sources and Analysis. NOAA Technical Memorandum NESDIS NGDC-24.  
651 <https://doi.org/10.7289/V5C8276M>
- 652 Ando, R., Nakata, R. & Hori, T., 2010. A slip pulse model with fault heterogeneity for low-  
653 frequency earthquakes and tremor along plate interfaces. *Geophys Res Lett*, **37**, 1–5.  
654 doi:10.1029/2010GL043056
- 655 Ando, R., Takeda, N. & Yamashita, T., 2012. Propagation dynamics of seismic and aseismic slip  
656 governed by fault heterogeneity and Newtonian rheology. *Journal of Geophysical Research*  
657 *B: Solid Earth*, **117**, Blackwell Publishing Ltd. doi:10.1029/2012JB009532
- 658 Aoi, S., Asano, Y., Kunugi, T., Kimura, T., Uehira, K., Takahashi, N., Ueda, H., *et al.*, 2020.  
659 MOWLAS: NIED observation network for earthquake, tsunami and volcano. *Earth, Planets*  
660 *and Space*, **72**, Springer Berlin Heidelberg. doi:10.1186/s40623-020-01250-x
- 661 Asano, Y., Obara, K., Matsuzawa, T., Hirose, H. & Ito, Y., 2015. Possible shallow slow slip events  
662 in Hyuga-nada, Nankai subduction zone, inferred from migration of very low frequency  
663 earthquakes. *Geophys Res Lett*, **42**, 331–338. doi:10.1002/2014GL062165
- 664 Baba, S., 2022. Spatiotemporal characteristics of slow earthquakes in subduction zones around  
665 Japan. PhD thesis of the University of Tokyo, Japan.
- 666 Baba, S., Obara, K., Takemura, S., Takeo, A. & Abers, G.A., 2021. Shallow Slow Earthquake  
667 Episodes Near the Trench Axis Off Costa Rica. *J Geophys Res Solid Earth*.  
668 doi:10.1029/2021JB021706
- 669 Baba, S., Takemura, S., Obara, K. & Noda, A., 2020. Slow Earthquakes Illuminating Interplate  
670 Coupling Heterogeneities in Subduction Zones. *Geophys Res Lett*, **47**, 4–5.  
671 doi:10.1029/2020GL088089
- 672 Bartlow, N.M., Miyazaki, S., Bradley, A.M. & Segall, P., 2011. Space-time correlation of slip and  
673 tremor during the 2009 Cascadia slow slip event. *Geophys Res Lett*, **38**, Blackwell  
674 Publishing Ltd. doi:10.1029/2011GL048714
- 675 Chesley, C., Naif, S., Key, K. & Bassett, D., 2021. Fluid-rich subducting topography generates  
676 anomalous forearc porosity. *Nature*, **595**, 255–260, Nature Research. doi:10.1038/s41586-  
677 021-03619-8
- 678 DeMets, C., Gordon, R.G., Argus, D.F. & Stein, S., 1994. Effect of recent revisions to the  
679 geomagnetic reversal time scale on estimates of current plate motions. *Geophys Res Lett*,  
680 **21**, 2191–2194. doi:10.1029/94GL02118
- 681 Dragert, H., Wang, K., James, T.S., 2001. A Silent Slip Event on the Deeper Cascadia Subduction  
682 Interface. *Science (1979)*, **292**, 1525–1528. doi:10.1126/science.1060152
- 683 Helffrich, G., Wookey, J., & Bastow, I. 2013. The Seismic Analysis Code. Cambridge: Cambridge

- 684 University Press. doi:10.1017/CBO9781139547260
- 685 Hirose, H., Hirahara, K., Kimata, F., Fujii, N. & Miyazaki, S., 1999. A slow thrust slip event  
686 following the two 1996 Hyuganada earthquakes beneath the Bungo Channel, southwest  
687 Japan. *Geophys Res Lett*, **26**, 3237–3240. doi:10.1029/1999GL010999
- 688 Houston, H., Delbridge, B.G., Wech, A.G., & Creager, K.C. 2011. Rapid tremor reversals in  
689 Cascadia generated by a weakened plate interface. *Nature Geoscience*, **4**, 404–409,  
690 doi:10.1038/NGE01157
- 691 Ide, S., 2016. Characteristics of slow earthquakes in the very low frequency band: Application to  
692 the Cascadia subduction zone. *J Geophys Res Solid Earth*, **121**, 5942–5952.  
693 doi:10.1002/2016JB013085
- 694 Ide, S. & Beroza, G.C., 2001. Does apparent stress vary with earthquake size? *Geophys Res Lett*,  
695 **28**, 3349–3352.
- 696 Ide, S. & Beroza, G.C., 2023. Slow earthquake scaling reconsidered as a boundary between  
697 distinct modes of rupture propagation. *Proc Natl Acad Sci U S A*, **120**, National Academy of  
698 Sciences. doi:10.1073/pnas.2222102120
- 699 Ide, S., Beroza, G.C., Shelly, D.R. & Uchide, T., 2007a. A scaling law for slow earthquakes.  
700 *Nature*, **447**, 76–79. doi:10.1038/nature05780
- 701 Ide, S., Imanishi, K., Yoshida, Y., Beroza, G.C. & Shelly, D.R., 2008. Bridging the gap between  
702 seismically and geodetically detected slow earthquakes. *Geophys Res Lett*, **35**, 2–7.  
703 doi:10.1029/2008GL034014
- 704 Ide, S. & Maury, J., 2018. Seismic Moment, Seismic Energy, and Source Duration of Slow  
705 Earthquakes: Application of Brownian slow earthquake model to three major subduction  
706 zones. *Geophys Res Lett*, **45**, 3059–3067. doi:10.1002/2018GL077461
- 707 Ide, S., Shelly, D.R. & Beroza, G.C., 2007b. Mechanism of deep low frequency earthquakes:  
708 Further evidence that deep non-volcanic tremor is generated by shear slip on the plate  
709 interface. *Geophys Res Lett*, **34**. doi:10.1029/2006GL028890
- 710 Ide, S. & Yabe, S., 2014. Universality of slow earthquakes in the very low frequency band.  
711 *Geophys Res Lett*, **41**, 2786–2793. doi:10.1002/2014GL059712
- 712 Igarashi, T., 2020. Catalog of small repeating earthquakes for the Japanese Islands. *Earth, Planets  
713 and Space*, **72**, Springer Berlin Heidelberg. doi:10.1186/s40623-020-01205-2
- 714 Ito, Y., Obara, K., Shiomi, K., Sekine, S. & Hirose, H., 2007. Slow Earthquakes Coincident with  
715 Episodic Tremors and Slow Slip Events. *Science (1979)*, **315**, 503–506.  
716 doi:10.1126/science.1134454
- 717 Kanamori, H. & Anderson, D.L., 1975. THEORETICAL BASIS OF SOME EMPIRICAL  
718 RELATIONS IN SEISMOLOGY. *Bulletin of the Seismological Society of America*, Vol. 65.  
719 Retrieved from <http://pubs.geoscienceworld.org/ssa/bssa/article->

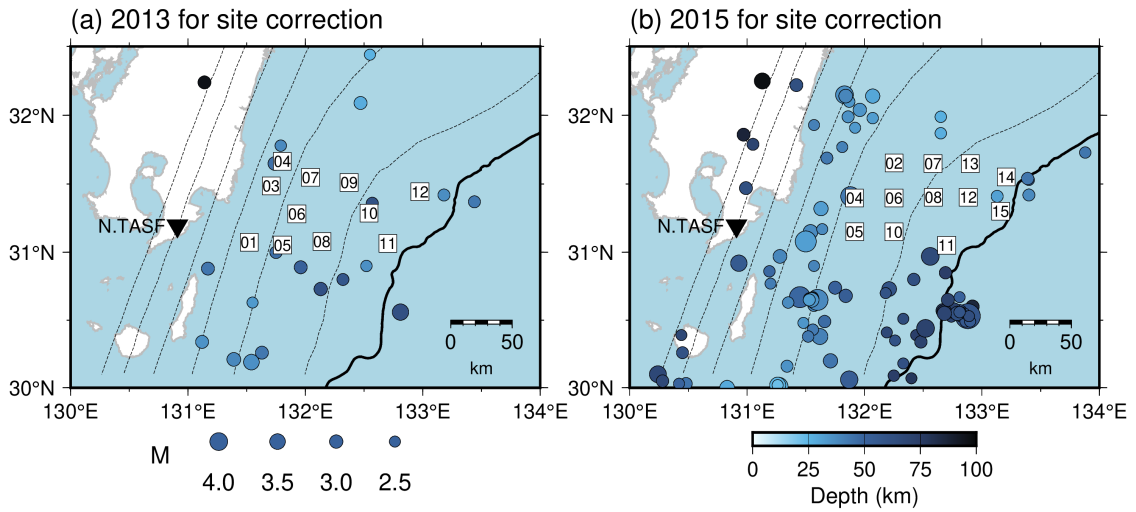
- 720 pdf/65/5/1073/5320189/bssa0650051073.pdf
- 721 Kanamori, H. & Rivera, L., 2006. Energy partitioning during an earthquake. *Geophysical*  
722 *Monograph Series*, **170**, 3–13. doi:10.1029/170GM03
- 723 Kaneko, L., Ide, S. & Nakano, M., 2018. Slow Earthquakes in the Microseism Frequency Band  
724 (0.1–1.0 Hz) off Kii Peninsula, Japan. *Geophys Res Lett*, **45**, 2618–2624.  
725 doi:10.1002/2017GL076773
- 726 Kano, M., Aso, N., Matsuzawa, T., Ide, S., Annoura, S., Arai, R., Baba, S., *et al.*, 2018a.  
727 Development of a Slow Earthquake Database. *Seismological Research Letters*, **89**, 1566–  
728 1575. doi:10.1785/0220180021
- 729 Kano, M., Kato, A., Ando, R. & Obara, K., 2018b. Strength of tremor patches along deep  
730 transition zone of a megathrust. *Sci Rep*, **8**, Nature Publishing Group. doi:10.1038/s41598-  
731 018-22048-8
- 732 Kato, A., Obara, K., Igarashi, T., Tsuruoka, H., Nakagawa, S. & Hirata, N., 2012. Propagation of  
733 Slow Slip Leading Up to the 2011 Mw 9.0 Tohoku-Oki Earthquake. *Science (1979)*, **335**,  
734 705–708. doi:10.1126/science.1215141
- 735 Koketsu, K., Miyake, H., Suzuki, H., 2012. Japan Integrated Velocity Structure Model Version 1.  
736 In: Proceedings of the 15th World Conference on Earthquake Engineering, Lisbon, Portugal,  
737 24-28 September, Paper 1773.
- 738 Maeda, T., Takemura, S. & Furumura, T., 2017. OpenSWPC: An open-source integrated parallel  
739 simulation code for modeling seismic wave propagation in 3D heterogeneous viscoelastic  
740 media 4. *Seismology. Earth, Planets and Space*, **69**, Springer Berlin Heidelberg.  
741 doi:10.1186/s40623-017-0687-2
- 742 Masuda, K., Ide, S., Ohta, K. & Matsuzawa, T., 2020. Bridging the gap between low-frequency  
743 and very-low-frequency earthquakes. *Earth, Planets and Space*, **72**, Springer Berlin  
744 Heidelberg. doi:10.1186/s40623-020-01172-8
- 745 Nadeau, R.M. & McEvilly, T. v, 1999. Fault Slip Rates at Depth from Recurrence Intervals of  
746 Repeating Microearthquakes. *A. A. Koulakov and B. I. Shklovskii Phys. Rev. B*, Vol. 27.
- 747 Nakanishi, A., Takahashi, N., Yamamoto, Y., Takahashi, T., Citak, S.O., Nakamura, T., Obana, K.,  
748 *et al.*, 2018. Three-dimensional plate geometry and P-wave velocity models of the  
749 subduction zone in SW Japan: Implications for seismogenesis. *Special Paper of the*  
750 *Geological Society of America*, **534**, 69–86, Geological Society of America.  
751 doi:10.1130/2018.2534(04)
- 752 Nakata, R., Ando, R., Hori, T. & Ide, S., 2011. Generation mechanism of slow earthquakes:  
753 Numerical analysis based on a dynamic model with brittle-ductile mixed fault heterogeneity.  
754 *J Geophys Res Solid Earth*, **116**, Blackwell Publishing Ltd. doi:10.1029/2010JB008188
- 755 National Research Institute for Earth Science and Disaster Resilience, 2019. NIED F-net.

- 756 doi:10.17598/NIED.0005
- 757 Obara, K., 2002. Nonvolcanic Deep Tremor Associated with Subduction in Southwest Japan.  
758 *Science (1979)*, **296**, 1679–1681. doi:10.1126/science.1070378
- 759 Obara, K. & Ito, Y., 2005. Very low frequency earthquakes excited by the 2004 off Kii peninsula  
760 earthquakes: A dynamic deformation process in the large accretionary prism. *Earth, Planets  
761 and Space*, **57**, 321–326. doi:10.1186/BF03352570
- 762 Obara, K. & Kato, A., 2016. Connecting slow earthquakes to huge earthquakes. *Science*, **353**,  
763 253–257. doi:10.1126/science.aaf1512
- 764 Ohta, K. & Ide, S., 2017. Resolving the Detailed Spatiotemporal Slip Evolution of Deep Tremor  
765 in Western Japan. *J Geophys Res Solid Earth*, **122**, 10,009–10,036.  
766 doi:10.1002/2017JB014494
- 767 Ruiz, S., Metois, N., Fuenzalida, A., Ruiz, J., Leyton, F., Grandin, R., Vigny, C., Madariaga, R.,  
768 & Campos, J. 2014. Intense foreshocks and a slow slip event preceded the 2014 Iquique Mw  
769 8.1 earthquake. *Science*, 345(6201), 1165–1169. doi:10.1126/science.1256074
- 770 Shelly, D.R., Beroza, G.C., Ide, S. & Nakamura, S., 2006. Low-frequency earthquakes in Shikoku,  
771 Japan, and their relationship to episodic tremor and slip. *Nature*, **442**, 188–191.  
772 doi:10.1038/nature04931
- 773 Takemoto, T., Furumura, T., Saito, T., Maeda, T. & Noguchi, S., 2012. Spatial- and frequency-  
774 dependent properties of site amplification factors in Japan derived by the coda normalization  
775 method. *Bulletin of the Seismological Society of America*, **102**, 1462–1476.  
776 doi:10.1785/0120110188
- 777 Takemura, S., Baba, S., Yabe, S., Emoto, K., Shiomi, K. & Matsuzawa, T., 2022a. Source  
778 Characteristics and Along-Strike Variations of Shallow Very Low Frequency Earthquake  
779 Swarms on the Nankai Trough Shallow Plate Boundary. *Geophys Res Lett*, **49**, John Wiley  
780 and Sons Inc. doi:10.1029/2022GL097979
- 781 Takemura, S., Matsuzawa, T., Noda, A., Tonegawa, T., Asano, Y., Kimura, T. & Shiomi, K., 2019.  
782 Structural Characteristics of the Nankai Trough Shallow Plate Boundary Inferred From  
783 Shallow Very Low Frequency Earthquakes. *Geophys Res Lett*, **46**, 4192–4201.  
784 doi:10.1029/2019GL082448
- 785 Takemura, S., Obara, K., Shiomi, K. & Baba, S., 2022b. Spatiotemporal Variations of Shallow  
786 Very Low Frequency Earthquake Activity Southeast Off the Kii Peninsula, Along the  
787 Nankai Trough, Japan. *J Geophys Res Solid Earth*, **127**, John Wiley and Sons Inc.  
788 doi:10.1029/2021JB023073
- 789 Takemura, S., Okuwaki, R., Kubota, T., Shiomi, K., Kimura, T. & Noda, A., 2020. Centroid  
790 moment tensor inversions of offshore earthquakes using a three-dimensional velocity  
791 structure model: slip distributions on the plate boundary along the Nankai Trough. *Geophys*

- 792 *J Int*, **222**, 1109–1125, Oxford University Press. doi:10.1093/gji/ggaa238
- 793 Tonegawa, T., Yamashita, Y., Takahashi, T., Shinohara, M., Ishihara, Y., Kodaira, S. & Kaneda,  
794 Y., 2020. Spatial relationship between shallow very low frequency earthquakes and the  
795 subducted Kyushu-Palau Ridge in the Hyuga-nada region of the Nankai subduction zone.  
796 *Geophys J Int*, 1542–1554, Oxford University Press. doi:10.1093/gji/ggaa264
- 797 Uchida, N. & Matsuzawa, T., 2011. Coupling coefficient, hierarchical structure, and earthquake  
798 cycle for the source area of the 2011 off the Pacific coast of Tohoku earthquake inferred  
799 from small repeating earthquake data. *Earth, Planets and Space*, **63**, 675–679, Springer  
800 Berlin. doi:10.5047/eps.2011.07.006
- 801 Uchida, N., Matsuzawa, T., Hasegawa, A. & Igarashi, T., 2003. Interplate quasi-static slip off  
802 Sanriku, NE Japan, estimated from repeating earthquakes. *Geophys Res Lett*, **30**, American  
803 Geophysical Union. doi:10.1029/2003GL017452
- 804 Voss, N., Dixon, T.H., Liu, Z., Malservisi, R., Protti, M. & Schwartz, S., 2018. Do slow slip events  
805 trigger large and great megathrust earthquakes? *Sci Adv*, **4**, 1–6. doi:10.1126/sciadv.aat8472
- 806 Wang, K. & Bilek, S.L., 2011. Do subducting seamounts generate or stop large earthquakes?  
807 *Geology*, **39**, 819–822, Geological Society of America. doi:10.1130/G31856.1
- 808 Wang, Q.-Y., Frank, W.B., Abercrombie, R.E., Obara, K. & Kato, A., 2023. P L A N E T A R Y S  
809 C I E N C E What makes low-frequency earthquakes low frequency. Retrieved from  
810 <https://www.science.org>
- 811 Wessel, P., Smith, W.H.F., Scharroo, R., Luis, J. & Wobbe, F., 2013. Generic mapping tools:  
812 Improved version released. *Eos (Washington DC)*, **94**, 409–410.  
813 doi:10.1002/2013EO450001
- 814 Yabe, S., Baba, S., Tonegawa, T., Nakano, M. & Takemura, S., 2021. Seismic energy radiation  
815 and along-strike heterogeneities of shallow tectonic tremors at the Nankai Trough and Japan  
816 Trench. *Tectonophysics*, 228714, Elsevier B.V. doi:10.1016/j.tecto.2020.228714
- 817 Yabe, S., Tonegawa, T. & Nakano, M., 2019. Scaled Energy Estimation for Shallow Slow  
818 Earthquakes. *J Geophys Res Solid Earth*, **124**, 1507–1519. doi:10.1029/2018JB016815
- 819 Yamamoto, Y., Ariyoshi, K., Yada, S., Nakano, M. & Hori, T., 2022. Spatio-temporal distribution  
820 of shallow very-low-frequency earthquakes between December 2020 and January 2021 in  
821 Kumano-nada, Nankai subduction zone, detected by a permanent seafloor seismic network.  
822 *Earth, Planets and Space*, **74**, 14. doi:10.1186/s40623-022-01573-x
- 823 Yamamoto, Y., Obana, K., Takahashi, T., Nakanishi, A., Kodaira, S. & Kaneda, Y., 2013. Imaging  
824 of the subducted kyushu-palau ridge in the hyuga-nada region, western nankai trough  
825 subduction zone. *Tectonophysics*, **589**, 90–102. doi:10.1016/j.tecto.2012.12.028
- 826 Yamashita, Y, Asano, Y., Shimizu, H., Uchida, K., Hirano, S., Umakoshi, K., Miyamachi, H., *et*  
827 *al.*, 2015. Migrating tremor off southern Kyushu as evidence for slow slip of a shallow

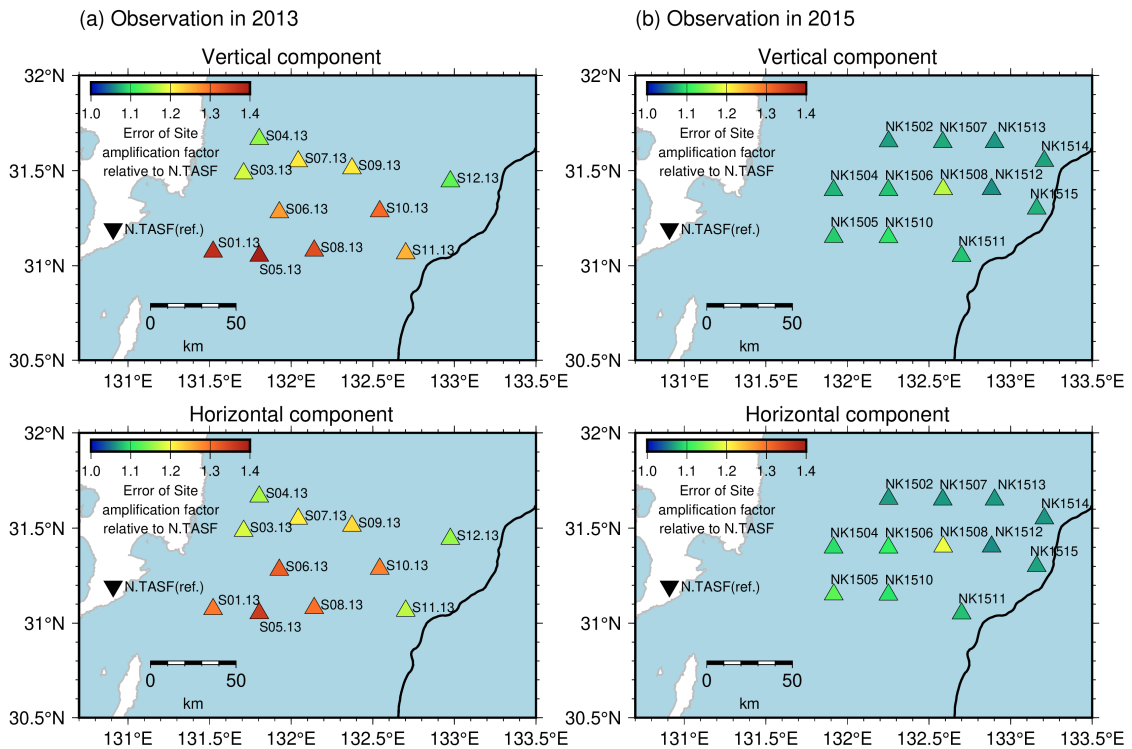
828 subduction interface. *Science (1979)*, **348**, 676–679. doi:10.1126/science.aaa4242  
829 Yamashita, Y., Shimizu, H. & Goto, K., 2012. Small repeating earthquake activity, interplate  
830 quasi-static slip, and interplate coupling in the Hyuga-nada, southwestern Japan subduction  
831 zone. *Geophys Res Lett*, **39**, Blackwell Publishing Ltd. doi:10.1029/2012GL051476  
832 Yamashita, Y., Shinohara, M. & Yamada, T., 2021. Shallow tectonic tremor activities in Hyuga-  
833 nada, Nankai subduction zone, based on long-term broadband ocean bottom seismic  
834 observations. *Earth, Planets and Space*, **73**, 196. doi:10.1186/s40623-021-01533-x  
835  
836





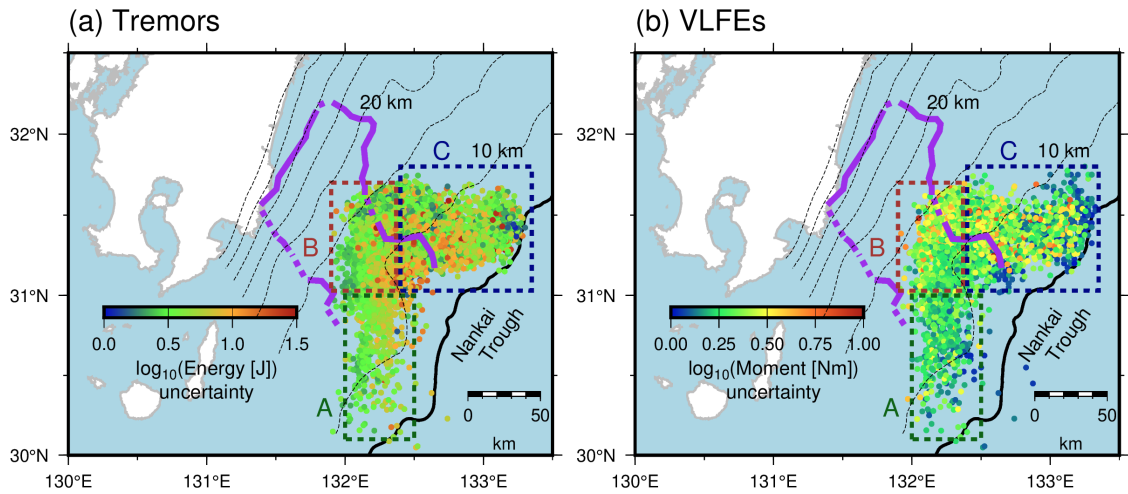
837  
838  
839  
840  
841

**Figure S1.** Distribution of earthquakes used for the estimation of the site amplification factors. Inverted triangles display the locations of the F-net stations. Squares represents the locations of OBSs. Black line and dotted contours are the same as displayed in Fig. 6.



842  
843  
844  
845  
846  
847

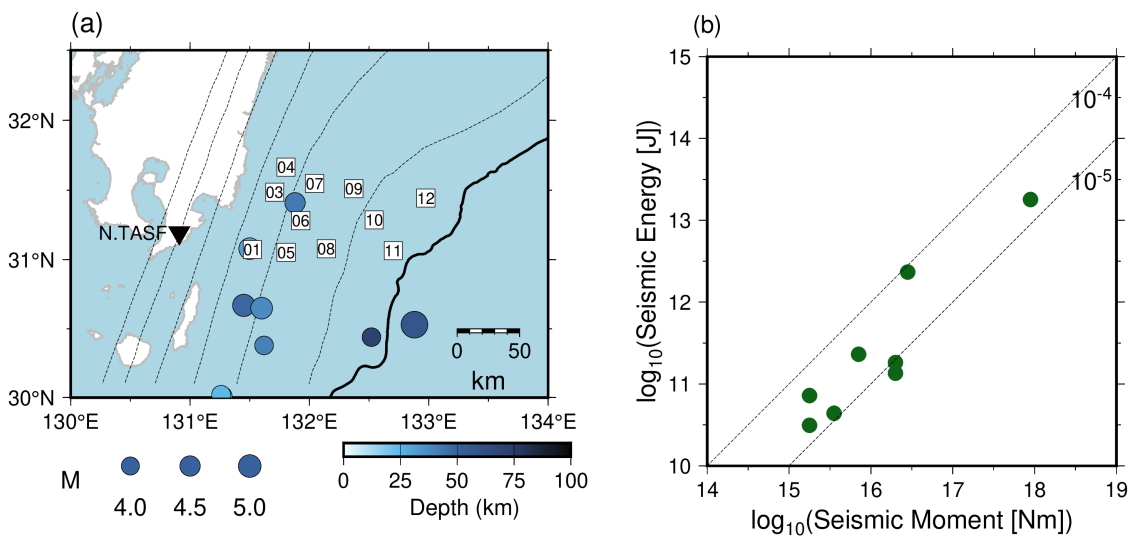
**Figure S2.** Estimation errors of site amplification factors relative to N.TASF at each OBS. Inverted triangle indicates the location of the F-net station, N.TASF. Black line is the same as displayed in Fig. 4.



848

849 **Figure S3.** Spatial distribution of the uncertainty of logarithm of (a) tremor energies and (b) VLFE  
 850 moments. Colored dotted rectangles, dashed contours, purple lines, black line and gray triangles  
 851 are the same as displayed in Fig. 7.

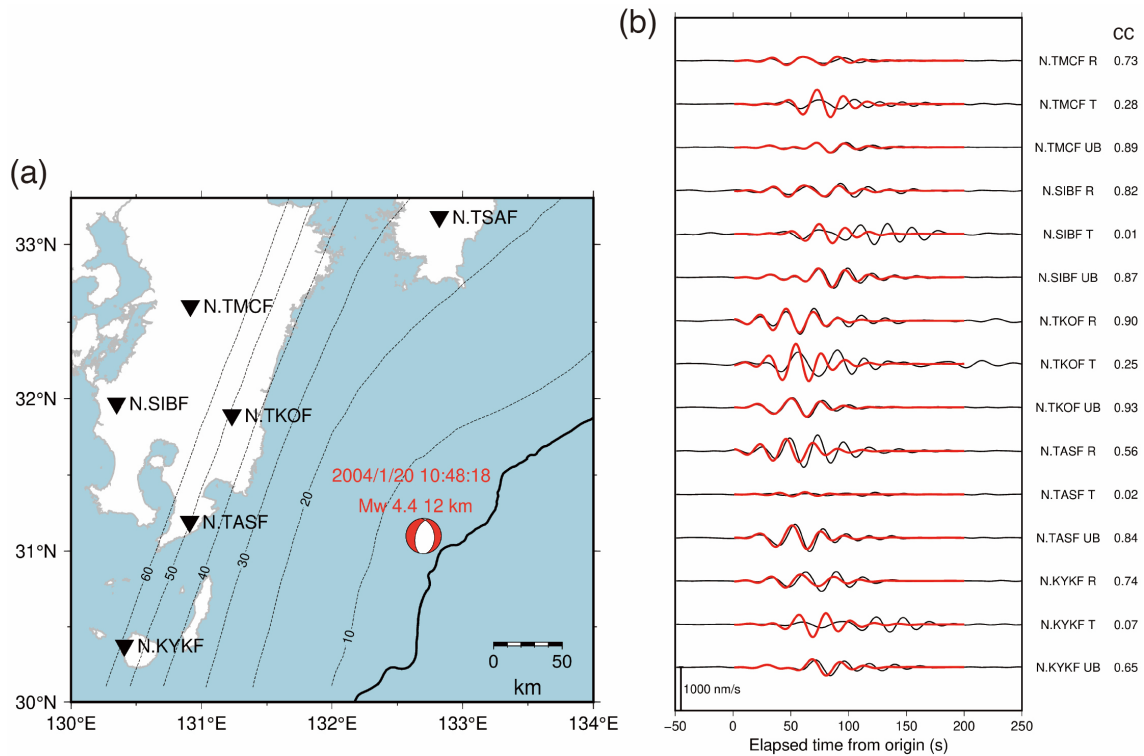
852



853

854 **Figure S4.** Estimation of seismic energies of regular earthquakes. (a) Distribution of regular  
 855 earthquakes used for the estimation of seismic energies. Squares are the same as displayed in Fig.  
 856 S1. Black line and dotted contours are the same as displayed in Fig. 6. (b) Relationship between  
 857 seismic moment and seismic energy of regular earthquakes shown in Fig. S4a. Seismic moments  
 858 are calculated from moment magnitude estimated by moment tensor analysis by F-net site  
 859 (<https://www.fnet.bosai.go.jp/event/search.php?LANG=en>). Dashed lines represent scaled  
 860 energies of  $10^{-5}$  and  $10^{-4}$ .

861



862

863

864

**Figure S5.** Simulated waveforms of a regular earthquake that occurred in northern Hyuga-nada.

865

(a) Focal mechanism of the regular earthquake listed in the catalog by Takemura et al. (2020;

866

catalog: doi:10.5281/zenodo.3821172). Black line, inverted triangles, and dotted contours are the same as displayed in Fig. 6. (b) Observed (black lines) and simulated (red lines) waveforms of

867

the earthquake at each F-net station. The assumed source time function was a Küpper wavelet

868

with a source duration of 1 s. Black and red lines are the observed and the simulated waveforms,

869

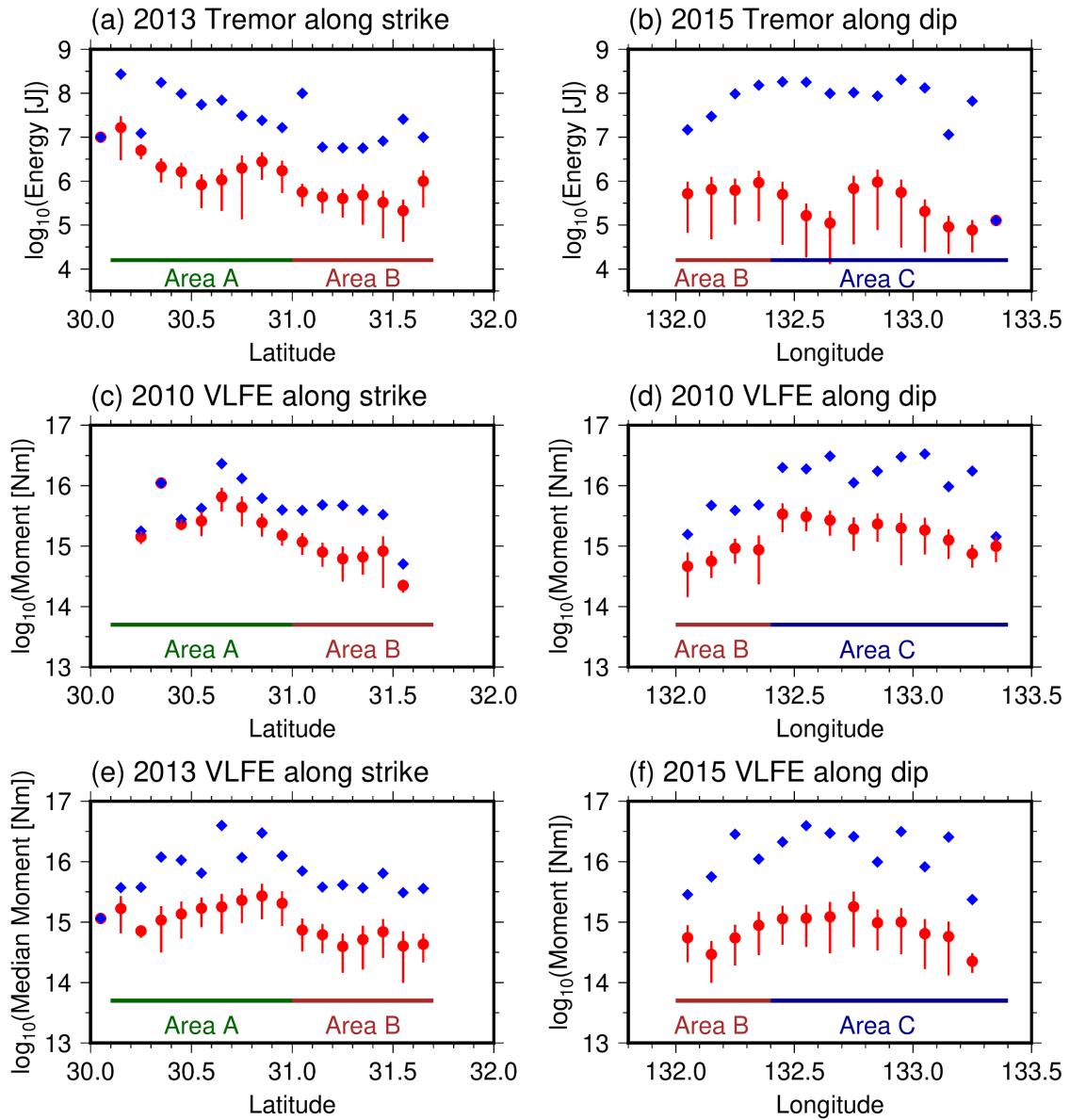
respectively. The simulation setting is the same as described in Section 2.2. R, T, and UB

870

components represent the radial, transverse, and vertical components, respectively.

871

872



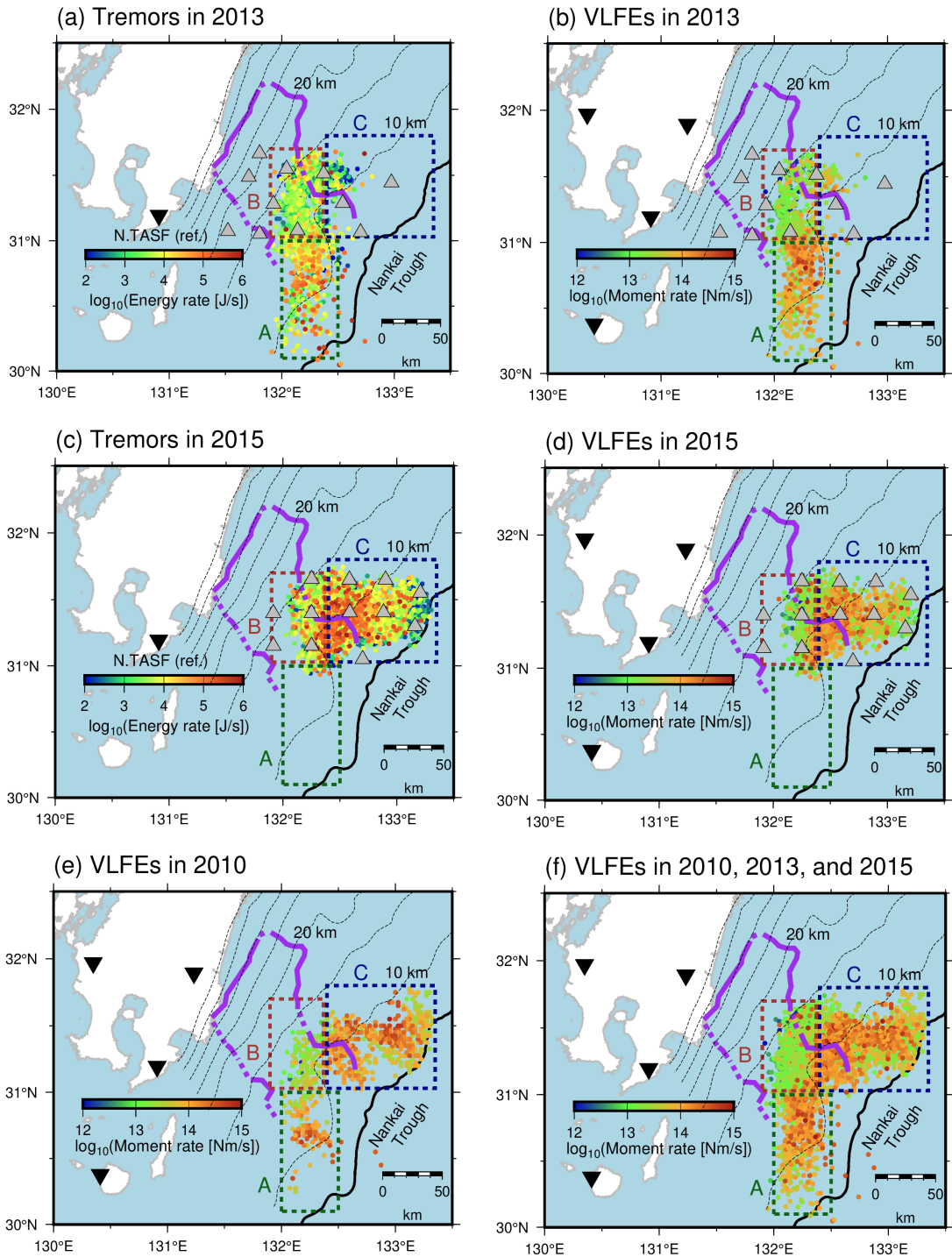
873

874

875 **Figure S6.** Variation in maximum and median of tremor energies and VLFE moments along strike  
 876 and dip directions at  $0.1^\circ$  interval. Blue diamonds and red circles represent the maximum and  
 877 median values, respectively. Red bars show the median absolute deviation of tremor energies and  
 878 VLFE moments.

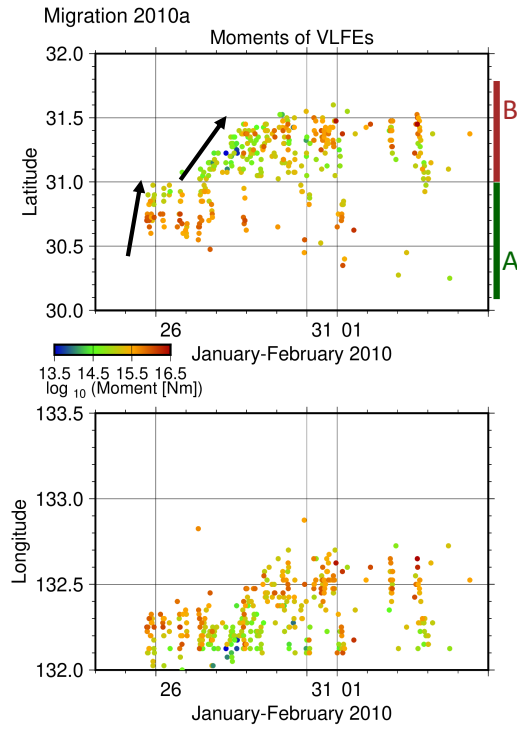
879

880



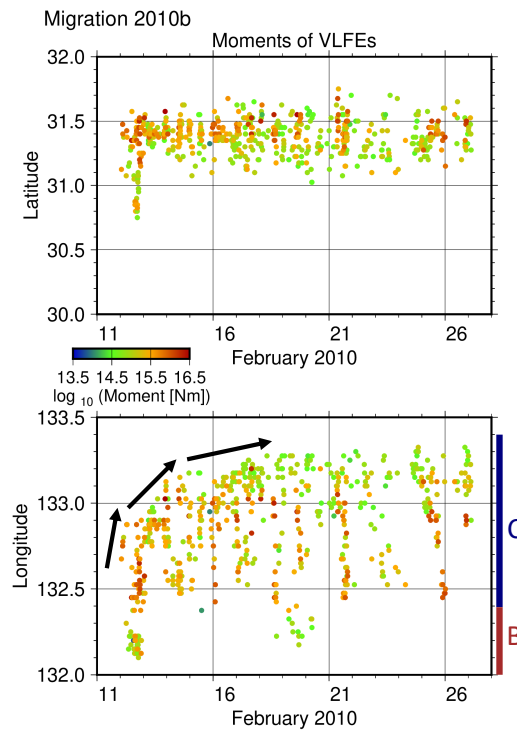
881

882 **Figure S7.** Spatial distribution of (a) energy rates of tremors in 2013, (b) moment rates of VLFs  
 883 in 2013, (c) energy rates of tremors in 2015, (d) moment rates of VLFs in 2015, (e) moment  
 884 rates of VLFs in 2010, and (f) moment rates of VLFs in all analysis periods. Colored dotted  
 885 rectangles, dashed contours, purple lines, black line and gray triangles are the same as displayed  
 886 in Fig. 7.



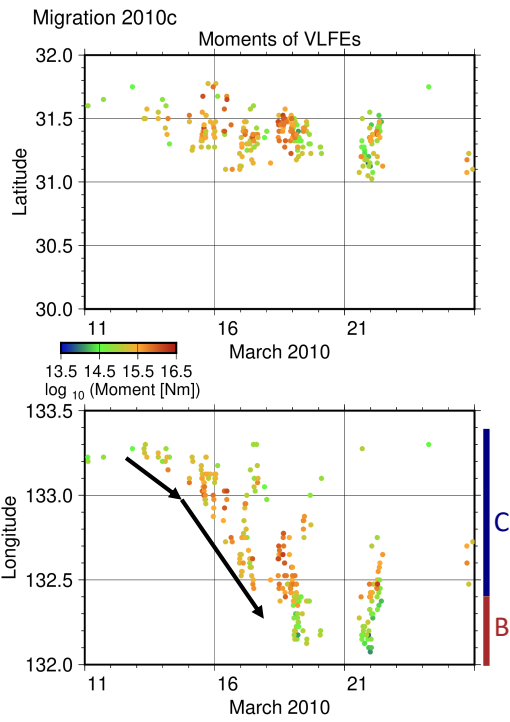
887

888 **Figure S8.** Spatiotemporal distributions of moments of VLFEs in the directions along the N-S  
889 and E-W sections for migration of 2010a migration. Black arrows indicate the direction of  
890 migrations.



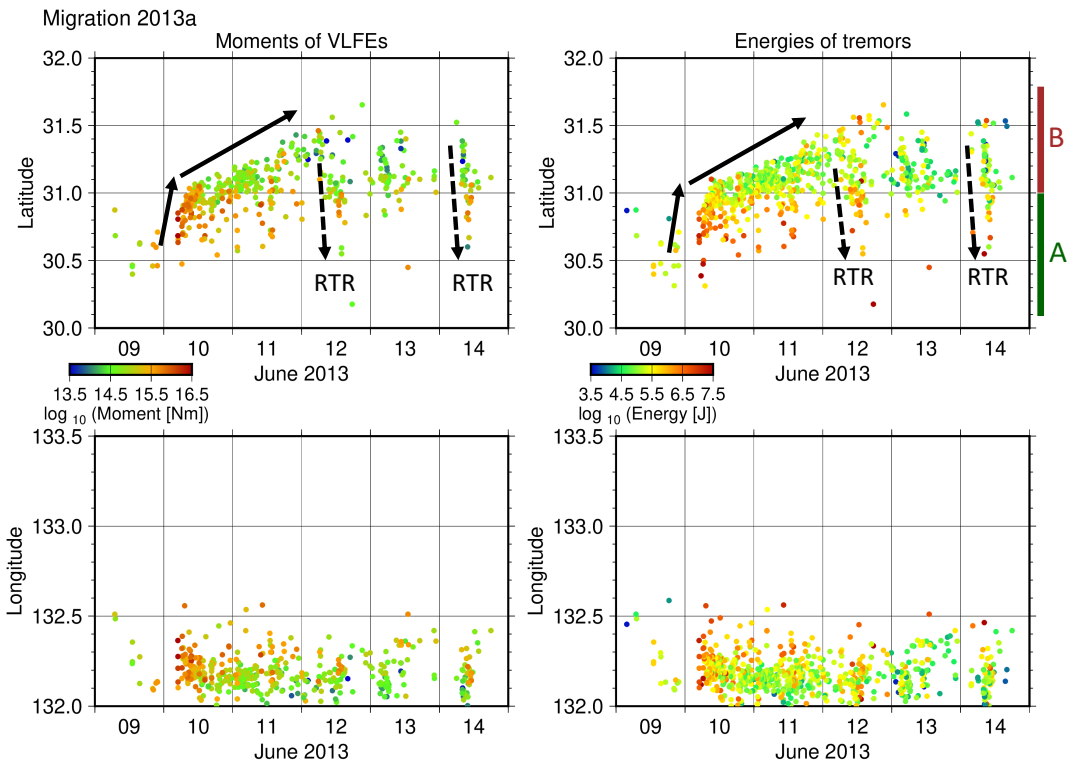
891

892 **Figure S9.** Same as Fig. S8 but 2010b migration.



893  
894  
895

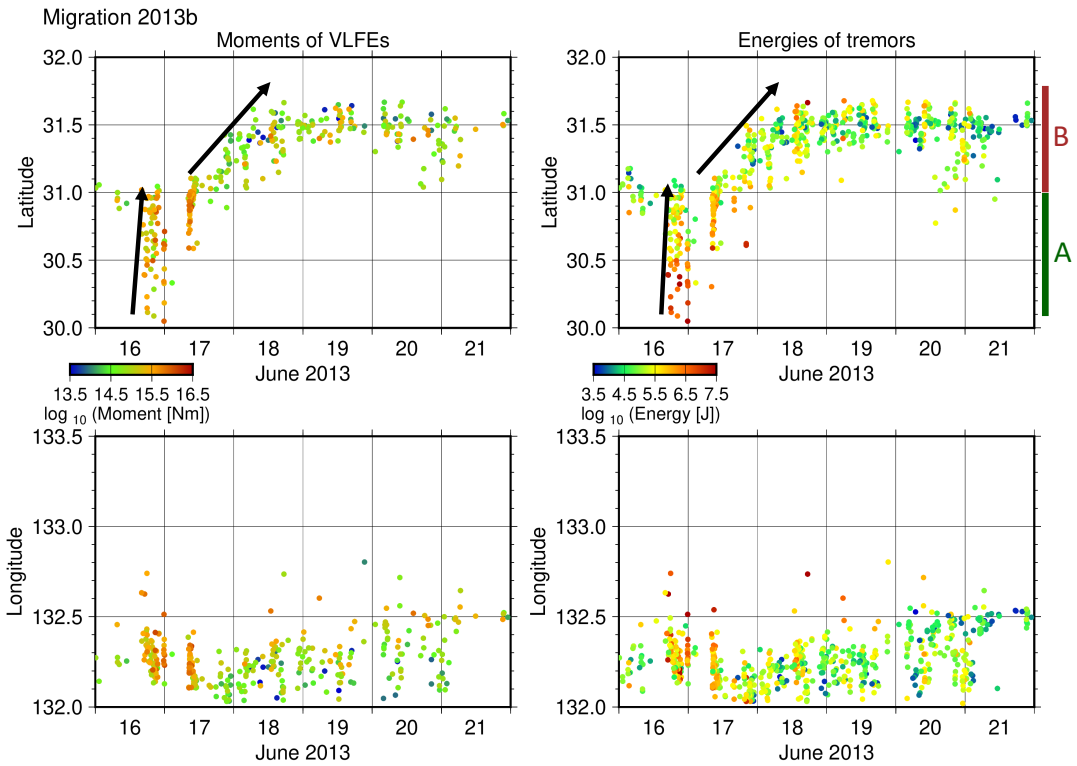
**Figure S10.** Same as Fig. S8 but 2010c migration.



896  
897  
898  
899

**Figure S11.** Spatiotemporal distributions of moments of VLFEs and energies of tremors in the directions along the N-S and E-W sections for migration of 2013a migration. Black dotted arrows represent the rapid tremor reversal (RTR).

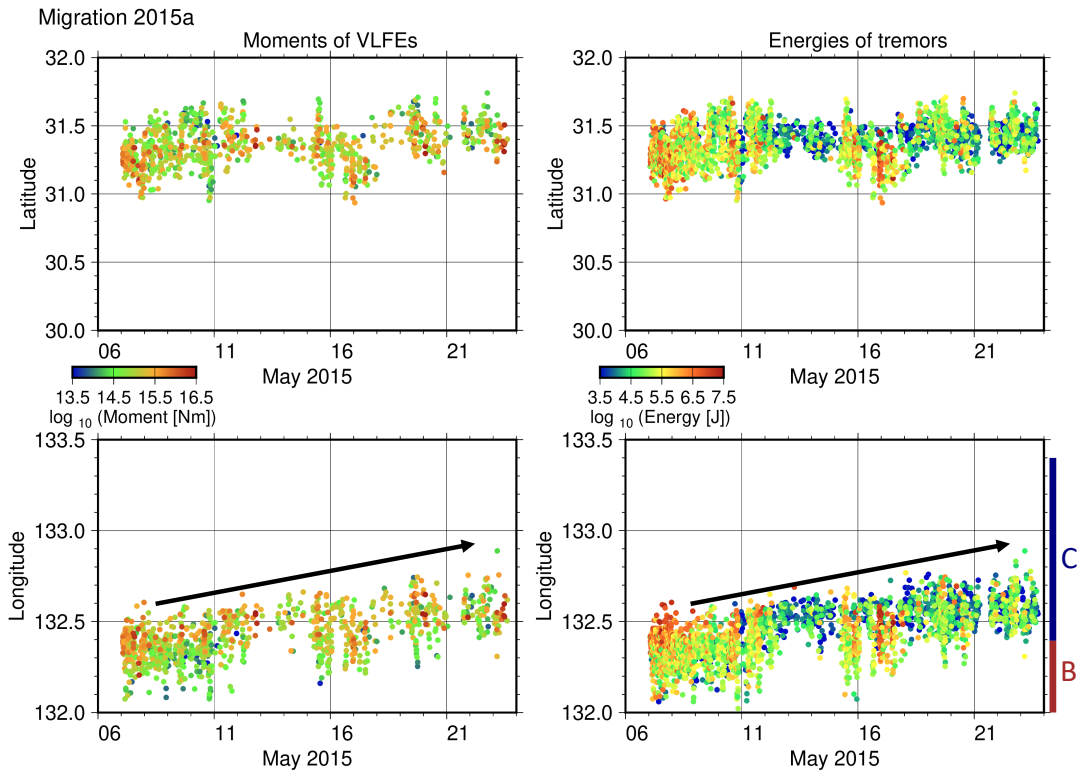




900

901 **Figure S12.** Same as Fig. S11 but 2013b migration.

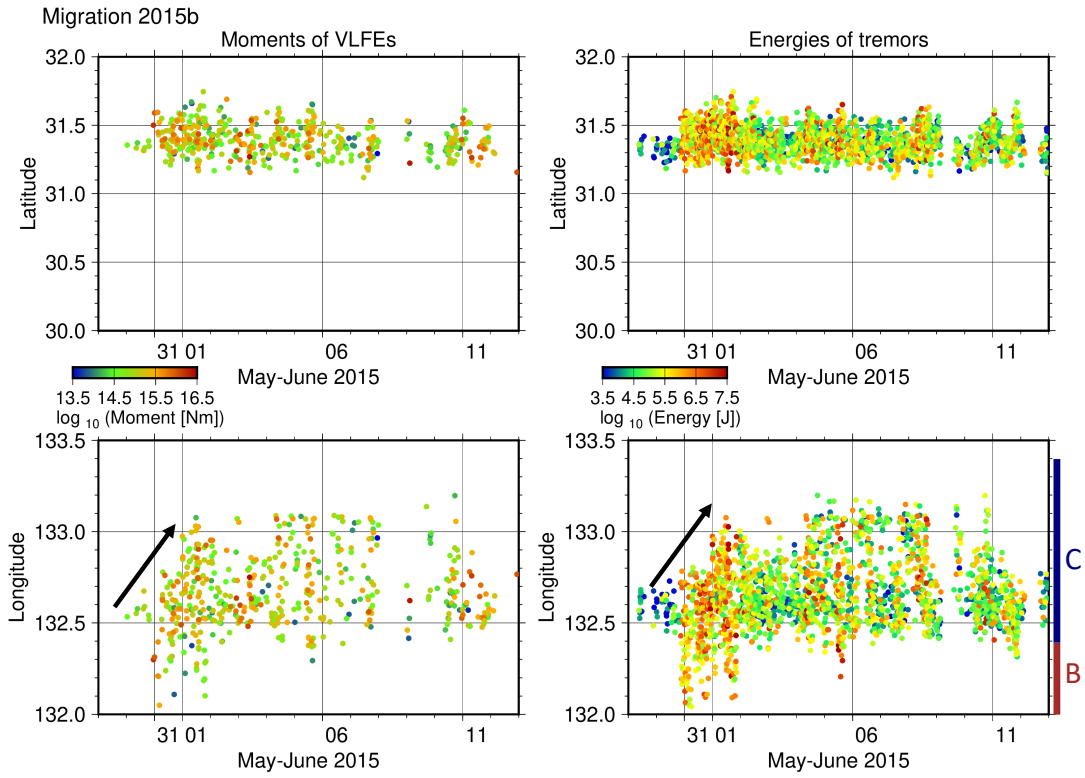
902



903

904 **Figure S13.** Same as Fig. S11 but 2015a migration.

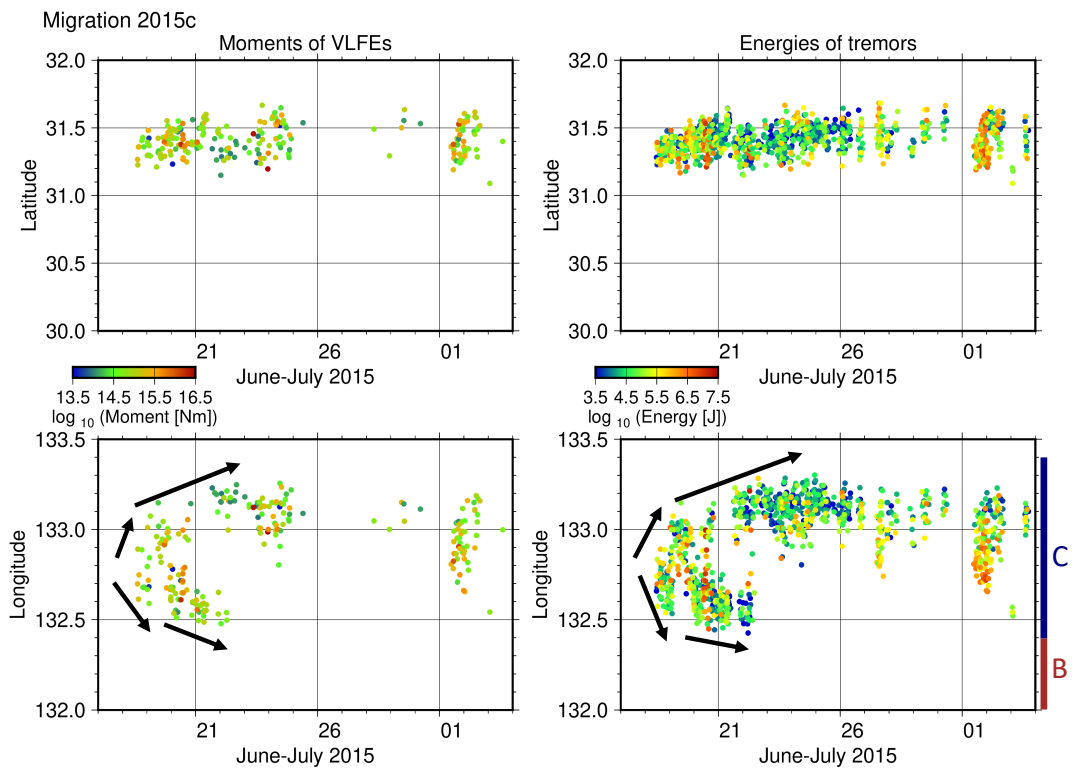




905

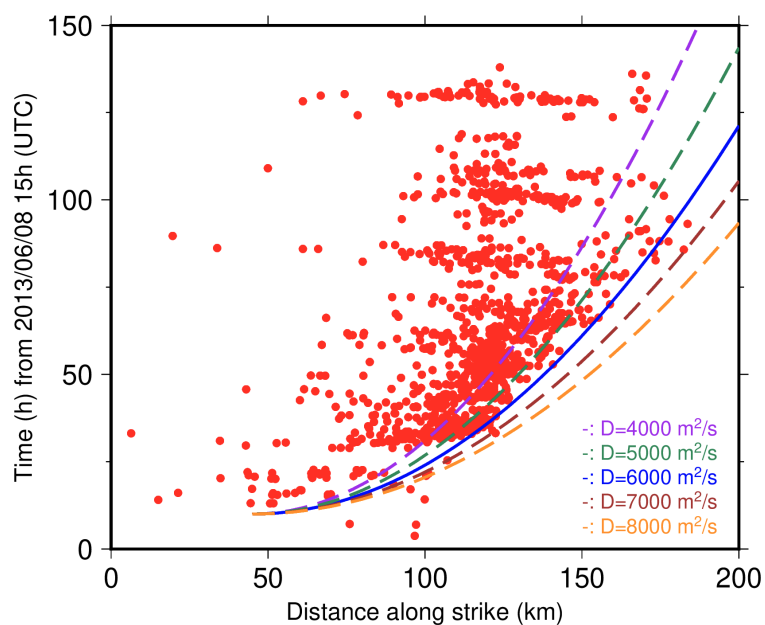
906 **Figure S14.** Same as Fig. S11 but 2015b migration.

907



908

909 **Figure S15.** Same as Fig. S11 but 2015c migration.



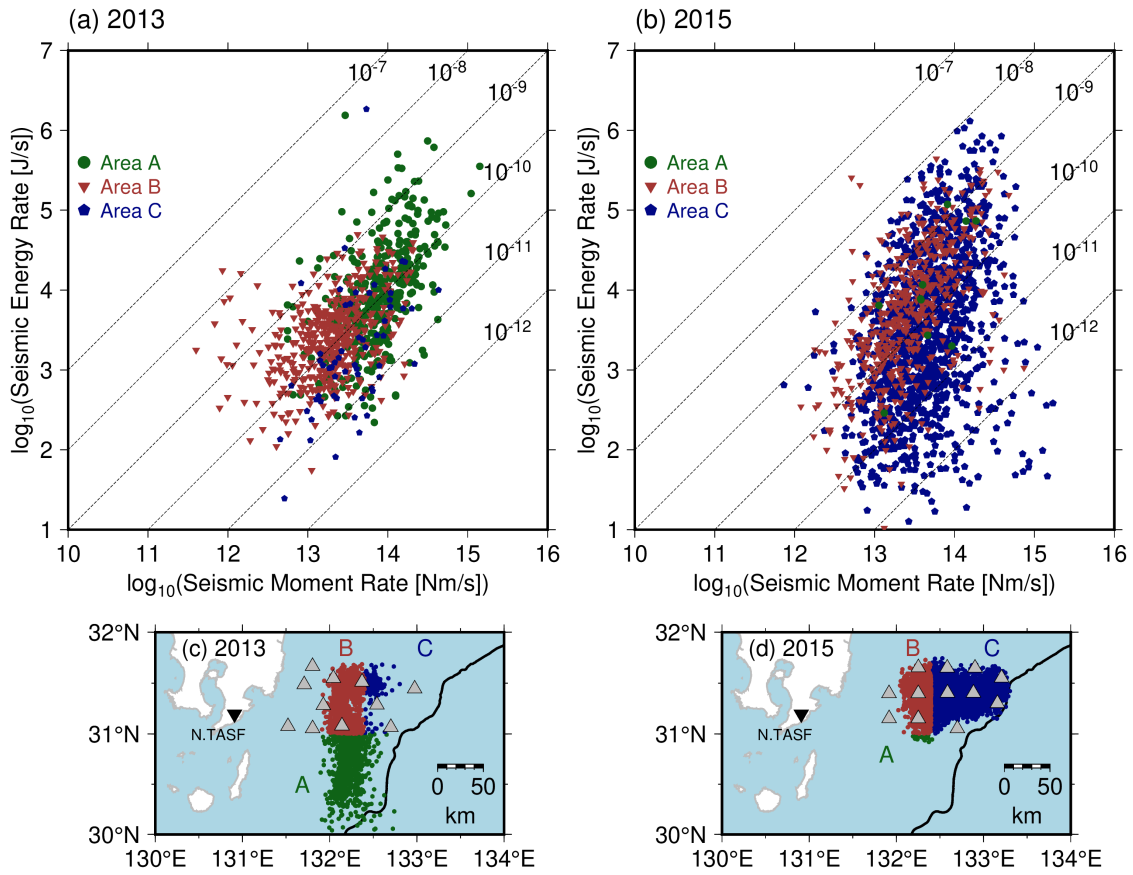
910

911 **Figure S16.** Same as Fig. 11 but with parabolic functions with diffusion coefficients  $D$  of  $4 \times 10^4$   
912  $\text{m}^2/\text{s}$ ,  $5 \times 10^4 \text{ m}^2/\text{s}$ ,  $6 \times 10^4 \text{ m}^2/\text{s}$ ,  $7 \times 10^4 \text{ m}^2/\text{s}$ , and  $8 \times 10^4 \text{ m}^2/\text{s}$ .

913

914

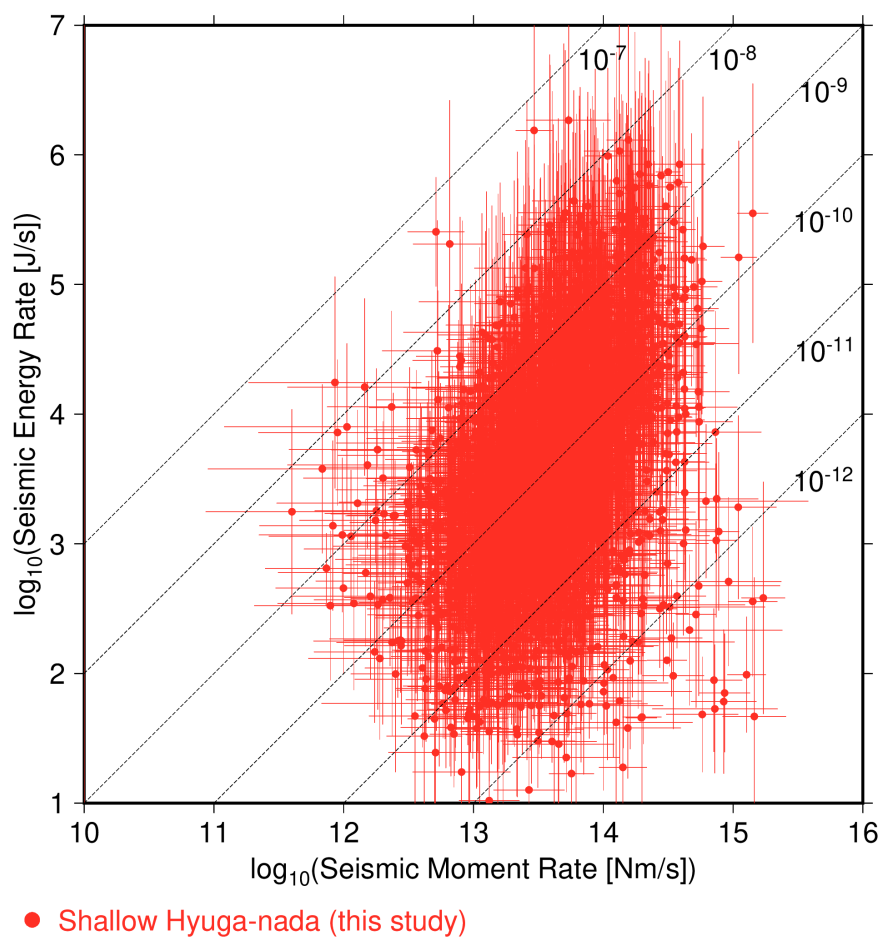
915



916

917 **Figure S17.** Relationship between seismic moment rates of VLFEs and seismic energy rates of  
 918 shallow tremors at each area in Hyuga-nada (a) in 2013 and (b) in 2015. Epicentres of shallow  
 919 tremors at each area (c) in 2013 and (d) in 2015. Shallow tremors in Area A, B, and C are depicted  
 920 by green, brown, and dark blue dots, respectively. Black lines, gray and black inverted triangles  
 921 are the same as displayed in Fig.7.

922

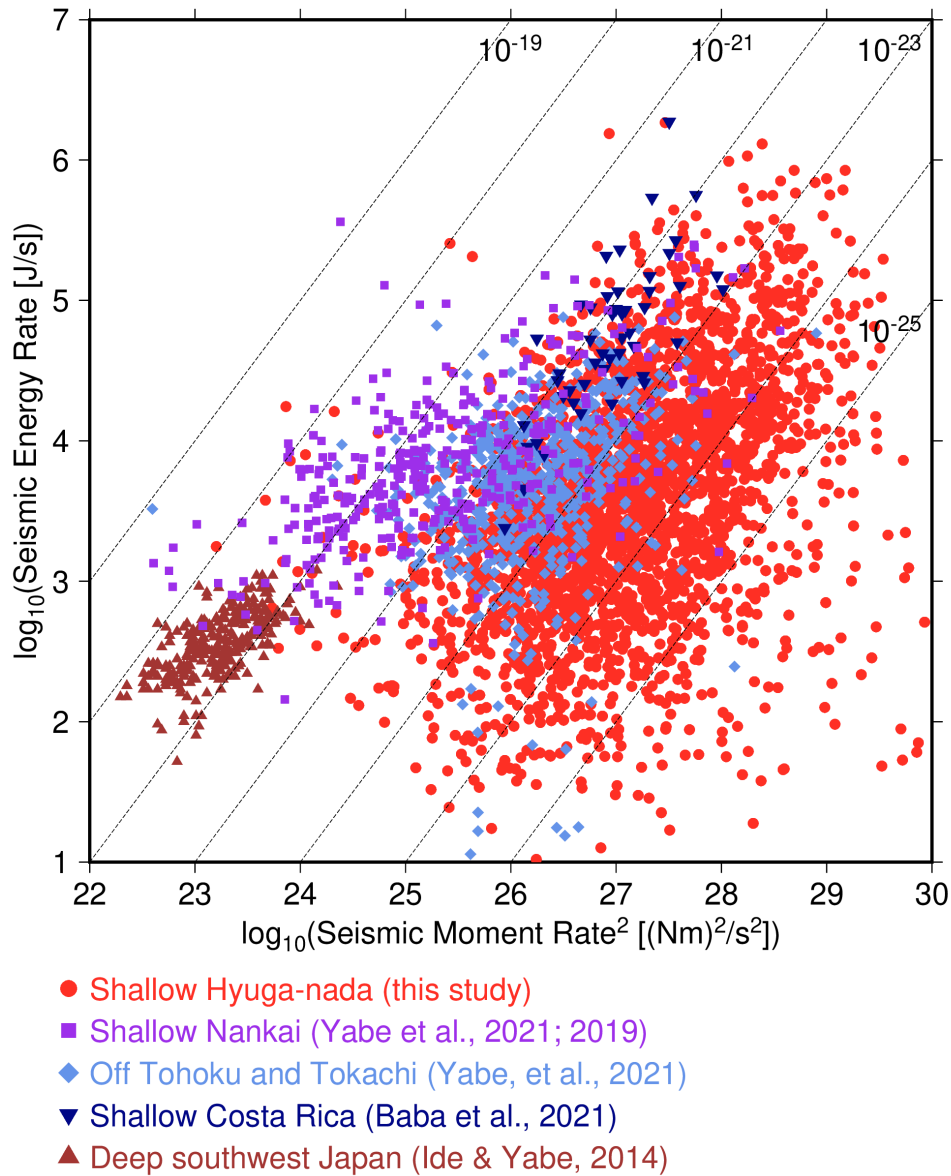


923

924 **Figure S18.** Relationship between seismic moment rates of VLFs and seismic energy rates of  
925 shallow tremors with error bars in Hyuga-nada.

926

927



928

929

930 **Figure S19.** Relationship between seismic moment rates of VLFs and squared seismic moment  
931 rates of tremors. Red circles, purple squares, green diamonds, dark blue inverted triangles, and  
932 dark blue triangles indicate the relationships between seismic moment rates of VLFs and seismic  
933 moment rates of tremors in shallow Hyuga-nada (this study), shallow Nankai except Hyuga-nada  
934 (Yabe et al. 2021, 2019), off Tohoku and Tokachi (Yabe et al. 2021), shallow Costa Rica (Baba et  
935 al. 2021), and deep slow earthquakes (Ide, 2016; Ide and Maury, 2018; Ide and Yabe, 2014).  
936

937 **Table S1.** Characteristics of migrations in Hyuga-nada.

938

Migration direction		
2010a	Along-strike	South to north
2010b	Along-dip	Downdip to updip
2010c	Along-dip	Updip to downdip
2013a	Along-strike	South to north
2013b	Along-strike	South to north
2015a	Along-dip	Downdip to updip
2015b	Along-dip	Downdip to updip
2015c	Along-dip	Bilateral

939

940